

# The Role of Gravity Waves in the Formation and Organization of Clouds During TWPICE

DE-SC0002521

Michael Reeder, Todd Lane, Mai Chi Nguyen Hankinson

One of the important features of the research is that it makes use of the observations of tropical convection taken during TWP-ICE, which are of unprecedented quality and scope. While the field experiment was not explicitly designed to examine research areas associated with convectively generated gravity waves, the observations taken are well suited nonetheless for such an investigation, especially in support of a program of numerical modelling. From this perspective the proposed research adds greater value to TWP-ICE. Another important feature of the research plan is that it strongly emphasises the synthesis and comparison of models with observation, making model evaluation one of the key components of the project. The results of this research are summarized below.

## 1. Analysis of Inertia-Gravity Waves

The results of this part of the project have been submitted for publication in the Journal of Geophysical Research [Hankinson, C. M. N., M. J. Reeder and T. P. Lane. 2013. Gravity waves generated by convection during TWP-ICE Part I: Inertia-gravity waves. *J. Geophys. Res.* (submitted)]. The main aim of this part of the project is to deduce the properties of low-frequency convectively generated gravity waves from the radiosonde observations made during TWP-ICE. The radiosonde soundings from five stations (Cape Don, Darwin, Garden Point, Mount Bundy and Point Stuart) are the main data used here. The vertical soundings of wind speed and direction, air temperature, mixing ratio, pressure and the altitude of the balloon are available every 3 hours with the time resolution of 2 seconds (except for Darwin where the soundings are only available every 6 hour). The zonal and meridional wind components ( $u$  and  $v$ , respectively) are derived from wind speed and direction. Subsequently, the profiles of horizontal wind components ( $u$  and  $v$ ), temperature  $T$ , mixing ratio  $q$  and pressure  $p$  are interpolated to a regular grid of 15 m resolution, up to a height of 30 km. As the tropopause is located near 17 km altitude during the campaign, most of the analysis of the data is confined to the altitude range 17.5 – 28 km. In addition, some analysis of high frequency waves use data from the troposphere, in the range 3-10 km altitude, which is the portion of the troposphere in which vertical temperature gradient is relatively constant.

The perturbations of  $u$ ,  $v$  and  $T$  (denoted as  $u'$ ,  $v'$  and  $T'$  respectively) are calculated by subtracting mean profiles. These mean profiles are constructed using the variational analysis from the observed profiles during the TWP-ICE campaign [Xie et al., 2010]. These profiles represent the time evolving spatial average conditions in a  $2 \times 2$  degree box centered on the campaign area. The basic assumption under-pinning the analysis is that these perturbations physically represent gravity waves. Two additional methods of defining the mean state were tested to access the sensitivity of the results to the choice of mean state. First, the mean state was defined as the time tendencies of the observations at each height. Second, the mean state was defined by a polynomial fitted to each vertical profile using least squares. Overall, the different mean states gave similar pattern of perturbations, although their magnitudes could be different by a few  $\text{m s}^{-1}$ .

Figure 1 shows the time-height evolution of the zonal wind perturbations at Point Stuart. The

evolution of the meridional wind (not shown) is similar to that of zonal wind. Likewise the temperature perturbations are similar with amplitude of about 10 K. The time-height evolution of the zonal wind perturbations show downward phase propagation, which is one of the characteristics of upward propagating gravity waves. Two distinct regimes are found, during which the propagating characteristics of the perturbations are quite different. The gravity waves in each regime have been analyzed separately.

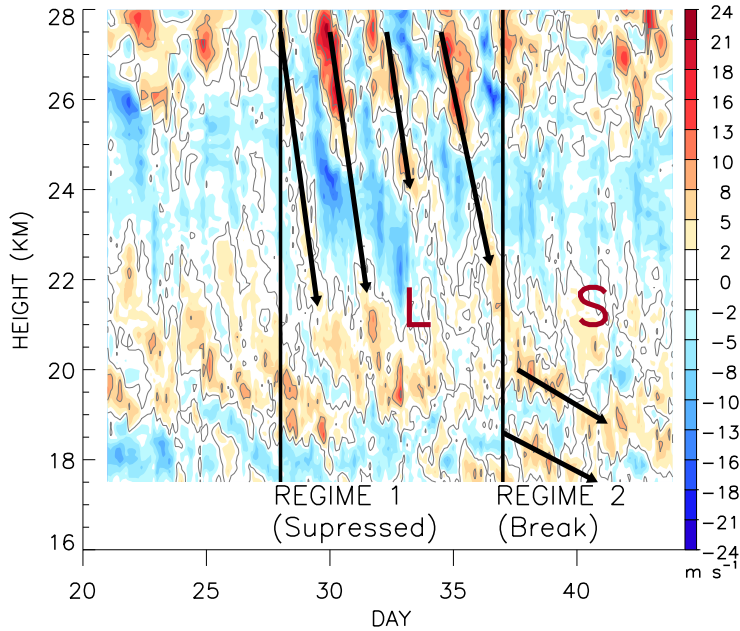


**Figure 1.** Time-height evolution of the zonal wind perturbations at the station Point Stuart. Positive values are contoured. The mean state is taken from the variational analysis. Arrows mark the descending phase propagation.

In the first regime (28 January – 6 February), large amplitude perturbations (of the order of 18 – 20  $\text{m s}^{-1}$ ) with clearly descending phase propagation are evident in the 22 - 28 km altitude range. This regime sits in the later part of the suppressed monsoon and the clear day periods identified by May et al. [2008]. The second regime (7 – 13 February) coincides with the monsoon break period. In this regime the downward phase propagation is most clearly evident below the heights of 22 km. Compared with the wave characteristics in Regime 1, these perturbations have smaller downward phase speeds and smaller vertical wavelengths. Although there are similar descending-phase perturbations in the lower stratosphere during Regime 1, they are dominated by the signals at the higher altitudes.

The ground-based frequency-vertical wavenumber quadrature power spectra are calculated (and averaged over all stations) for the horizontal wind perturbations during Regimes 1 and 2. The quadrature spectra are defined using Fourier analysis as the imaginary part of cross spectrum of the two horizontal components of the velocity. During Regime 1, the quadrature spectrum for waves of group L peaks at a ground-based period of 2.3 days and vertical wavelength of 5.2 km. During Regime 2, waves of group S have a ground-based period near 3.5 days and the vertical wavelengths in the range of 1.5 to 2.1 km. The properties of waves of groups L and S noted above are consistent with the phase lines marked by the arrows in Fig. 1.

Wave groups L and S are further investigated by backward ray tracing to understand their origins and association with convective sources. For this purpose, the program suite GROGRAT, which is developed and described by Marks and Eckermann [1995], is employed using wind and temperature fields from the 6-hourly ERA Interim reanalysis. The type of convection along each ray is identified following the method of Inoue [1987] using hourly infrared satellite data from MTSAT. The presence of convection in each section between two consecutive points along the ray is defined if the area covered by convection is at least 10% in a  $2 \times 2$  degree box centered at the middle of the section. In the case of long sections, the box is expanded to fit the whole section. Figure 2 shows rays from group L traced backward from 00 UTC 04 February. The rays originate mainly from the area 123 E – 127 E and 7 S – 0.5 S near Indonesia where deep convection is analyzed. While passing this deep convection region, the rays are in the middle troposphere from 3 – 17 km (not shown). Thus, it appears that these waves were generated by deep convection in this region.

## 2. Analysis of High-Frequency Gravity Waves

This results from this part of the project have been reported in a paper submitted to the Journal of Geophysical Research [Hankinson, C. M. N., M. J. Reeder and T. P. Lane. 2013. Gravity waves generated by convection during TWP-ICE. Part II: High-frequency waves. *J. Geophys. Res.* (submitted)]. In general, high-frequency gravity waves are difficult to observe, as they tend to propagate rapidly upwards. Consequently, these waves are most commonly observed near the place and time of their generation. High-frequency gravity waves have been observed with radars and satellites. From radar data, the horizontal wavelength and frequency of the waves can be observed directly. The area covered by the radar, however, limits these data. From satellite data (e.g. airglow images), the horizontal wavelength and ground-based phase velocity are observed directly. Although satellites cover large areas, the observations of the high-frequency gravity waves are contingent on the waves reaching the upper atmosphere (e.g. at 80 – 100 km altitudes).

Using radiosonde data, Lane et al [2003], Geller and Gong [2010] and Gong and Geller [2010] deduced the wave activity and frequencies of the high-frequency gravity waves. Radiosonde data are available globally and for long times, but they are limited by relatively coarse time resolution (typically 3 to 12 hours between two consecutive observations). Moreover, the vertical wavelengths cannot be calculated from the sounding directly (Lane et al. [2003]). For all these reasons, there is a need for detailed observation of high-frequency gravity waves. The main aspects of the high-frequency gravity waves addressed here include their vertical and temporal variations, and their relationship with the rain rate, which is a proxy for the diabatic heating rate.

In the high-frequency range, properties of gravity waves are determined using perturbations of the vertical velocity derived from balloon's ascent rates [Lane et al., 2003]. The intrinsic period of these waves are found to be in the range of 20 – 40 minutes using the perturbation energy method of Geller and Gong [2010].

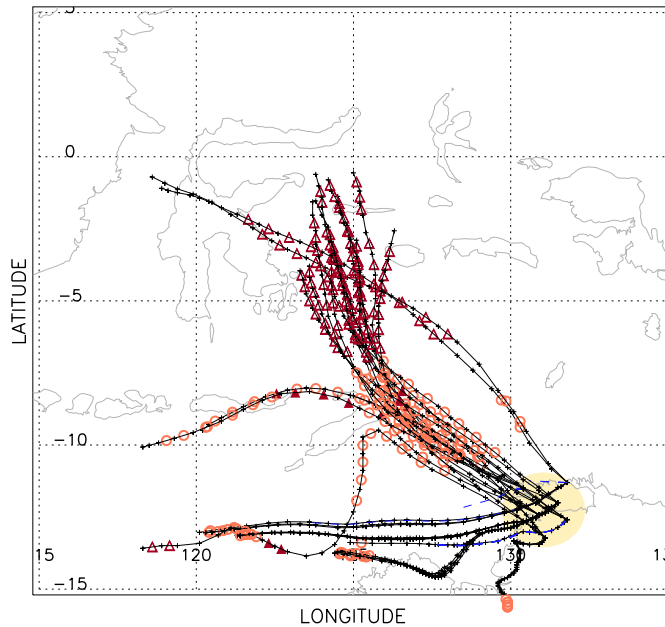


**Figure 2.** Backward ray tracing for groups L (arriving at 00Z 04/02/2006). Horizontal plane view. Black solid (dashed blue) lines show rays that do (do not) pass over regions with convective activity of deep (red triangles) and/or shallow (brown circles) convection. Shaded areas show the radar coverage during TWICE. Distance is calculated from the location of C-Pol radar at (131.044° E, 12.249° S).

Figure 3 shows the time-height evolution of the wave activity  $\rho w^2$  (derived from the ascent rate) averaged over all stations during Regimes 1 and 2. The strongest wave activity is concentrated in the layer below 22 km, indicating that the layer above filters the waves. Furthermore, the time series of the wave activity averaged over heights of 17.5 – 28 km exhibits a pulse-like pattern. This temporal variation of the 17.5 – 28 km mean wave activity is analyzed using a Morlet wavelet transform. During Regime 1, the wave activity varies predominantly with a 3 – 4 day period, but varies mostly with a 1-day period during Regime 2. While the 1-day period variation of the high-frequency gravity wave activity can be explained by the diurnal variation of the convection during the monsoon break (Regime 2), the origin of the 3 – 4 day variation during Regime 1 is related to the passage of tropical synoptic systems.

Precipitation estimates from C-pol radar are available every 10 minutes on a  $2.5 \times 2.5$  km grid. In addition to the rainfall rates, rainfall type (either convective, stratiform or mixed), determined by the method developed by Steiner et al. [2004], is available at each gridpoint. The rainfall and area for each type are accumulated over the 3-hour periods centered at the observation times. These data have been used to relate the activity of high frequency waves to the diabatic heating implied by rainfall.

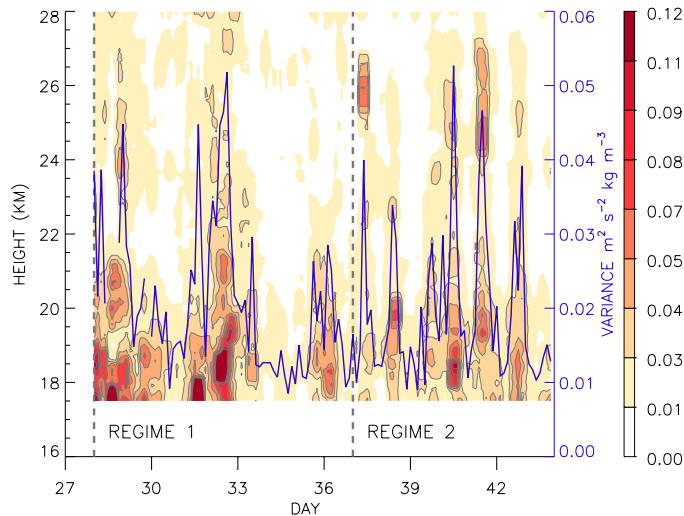


**Figure 3.** Evolution of high-frequency wave activity  $pw^2$  in the stratosphere.

The relationship between the wave activity and rain rate, which is a proxy for the diabatic heating by convection, is not a simple positive relation. At low rain rates, the wave activity increases as the rain rates increase, whereas there is no clear relationship between them at high values of rain rates associated with deep convective clouds. This result implies that diabatic heating, which is largely assumed as the main mechanism for gravity waves generation by convection, is not the only mechanism generating, especially for deep, precipitating convection.

The 3 – 4 day modulation of the wave activity during the suppressed monsoon regime and its concentration in the lower part of the stratosphere is investigated further by examining the propagation properties of the medium and the variation of the wave source. It is found that the propagation properties (namely the Scorer parameter) of the layer between 22 – 26 km are do not permit the transmission of short waves propagating to the east (upstream). Thus, the presence of this layer is consistent with the decrease of the wave activity with height. However, the variation in the propagation properties of the medium cannot explain for the 3 – 4 day period variation of the wave activity. Instead, the 3 – 4 day variation is consistent with the variation of the convection in the region within 300 km of the TWP-ICE domain.

### 3. WRF Simulations of the Convection and the Associated Waves Field

The convection and gravity waves observed during TWP-ICE are simulated with the Weather Research and Forecasting (WRF) Model (Skamarock *et al.* 2005). These simulations are compared with radiosonde observations described above and are used to determine some of the properties of convectively generated gravity waves. The results from this part of the project are currently being written up for publication in the Journal of Geophysical Research.

The model is configured as follows. There are 140 vertical levels to a height of 1 hPa, high resolution in the stratosphere, a 15 km damping layer at the top, 4 nested, two-way interacting grids with the horizontal spacings of 33 km, 11 km, 3.7 km and 1.2 km respectively. Figure 4a shows the arrangement of model grids. The physics options are: Thompson microphysics, Kain-Fritsch convective scheme for the outer two domains only, the RRTM scheme for long wave radiation, the

Dudhia scheme for short wave radiation, a Monin-Obukhov surface layer, and the unified Noah land-surface model. The initial and boundary conditions come from the ERA-Interim re-analyses.

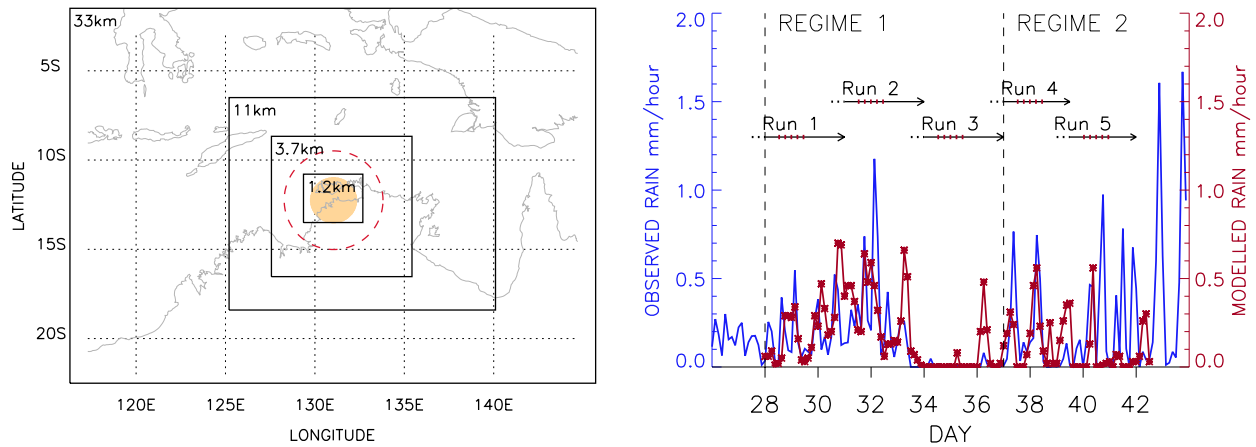


**Figure 4.** a) Simulation domains. Shaded area indicates the area covered by the radar during TWPICE. b) Simulated (red line with asterisks) and observed (blue solid line) rainfall averaged over the radar area.

Five overlapping simulations are conducted covering the period from 1200 UTC 27 January to 0000 UTC 12 February 2006 (see arrows in Fig. 4b). Each simulation is integrated for 3 days and 12 hours, the first 12 hours of which overlap with the previous simulation. These periods of overlap cover the model spin up and are not analysed. Figure 4b shows that the simulated precipitation averaged over radar area compares well with the observations albeit with smaller peaks.

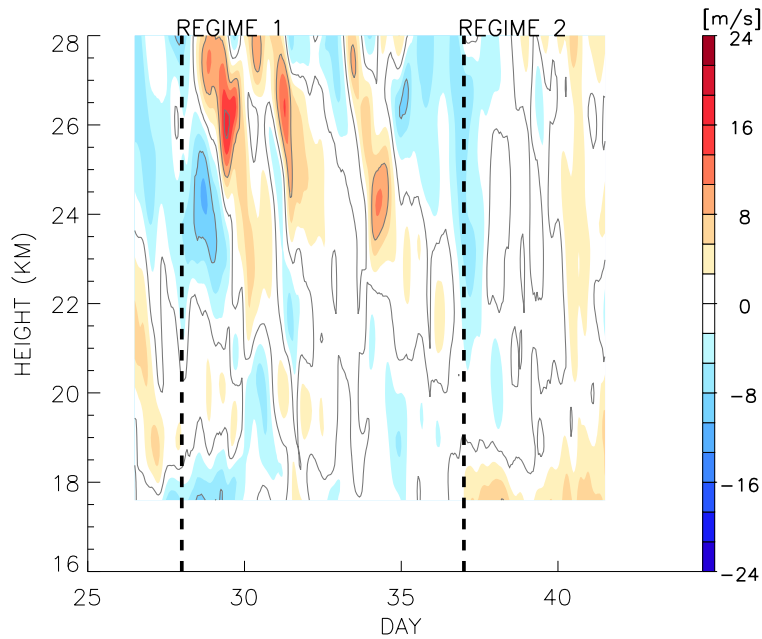


**Figure 5.** Time-height evolution of the simulated zonal wind perturbations at the station Point Stuart by the innermost grid.

The low-frequency inertia-gravity waves appear to be well simulated by the model. Figure 5 shows, similar to Fig. 1, the evolution of the zonal wind perturbations simulated by the model. Wave group L can be seen clearly with descending phase lines during the suppressed monsoon period. The phase lines, however, corresponding to wave group S are not shown clearly by the model simulation.

The high-frequency gravity waves simulated by the model are analysed by examining the vertical velocity field. During the suppressed monsoon regime, relatively linear wave fronts suggest that the gravity waves were generated elsewhere and propagate into the domain. In contrast, during the monsoon break regime, short horizontal wavelengths with circular wave fronts indicate that these gravity waves were generated by local convection within the domain.

The high-resolution model simulations provide a more complete picture of the wave field than that provided by the radiosonde profiles. For example, the horizontal wavelength and phase speeds of the high-frequency gravity waves can be determined. Figure 6 shows the zonal wavenumber-frequency spectra of vertical velocity at 22 km on day 32 (during the suppressed monsoon) and on day 38 (during the monsoon break). On day 32 (panel a), the dominant wave has a horizontal zonal wavelength of about 40 km, a period between 30 minutes and 1 hour, a vertical wavelength of about 8 km and propagates eastwards with the intrinsic speed of  $55 \text{ ms}^{-1}$ . In contrast, on day 38, the dominant waves have smaller horizontal wavelengths, between 7 and 20 km, periods between 30 minutes and 1 hours, vertical wavelengths less than 2 km, and propagate to both the east and west. These properties are consistent with the waves generated within the model domain and propagating outwards from their source.

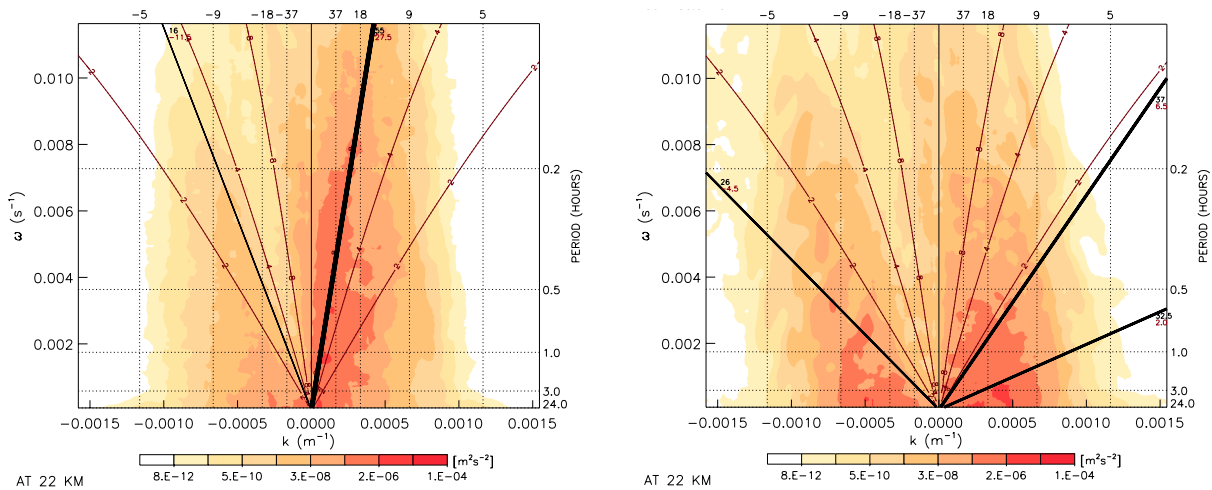


**Figure 6.** a) Zonal wavenumber-frequency spectra of the vertical velocity at 22 km during a) the suppressed monsoon (day 32) and b) the monsoon break (day 38). Black lines show zonal phase speeds, red thin lines indicate vertical wavelengths in km.

Figure 7 shows the relationship between the wave activity and the rainfall simulated by the model. The variation of the wave activity is closely related to the variation of rainfall (Fig. 7a). Furthermore, the scatter plot (Fig. 7b) shows a linear relationship between the wave activity and the rain rate during the suppressed monsoon period (blue bars). However, the wave activity appears to be independent of the rain rate at high rain rates during the monsoon break (red triangles). This result is consistent with the radiosonde observations. Moreover, the wave activity is independent of the rain rate over land during the monsoon break, which is consistent with the independence found in the observations for deep convective clouds.

Despite the agreement between the observed and simulated precipitation and its relationship with the wave activity, there are some notable differences between the model and observations. First, the simulated wave activity is roughly an order of magnitude less than the estimates derived from the radiosonde ascent rates. Second, the reduced wave activity in the 24 – 26 km layer is not captured in the model simulation. Third, the 3 – 4 day variation signal of the wave activity during the suppressed monsoon, although present, does not appear as strong as in the observations.

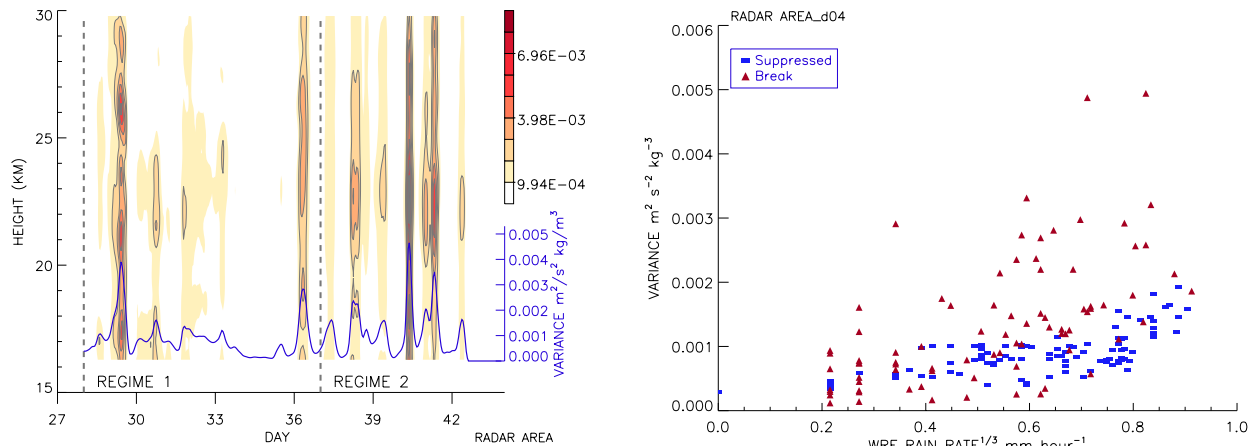


**Figure 7.** a) Time-height evolution of the wave activity simulated by the model. Blue line shows the averaged wave activity in the layer 17.5 – 28 km. b) Scatter plot of the wave activity against rain rate during suppressed monsoon (blue bars) and monsoon break (red triangles).

### Formation of Cirrus

This part of the project is progressing and will be completed in the next few months. During TWPICE, cirrus covered the Darwin area in the first half of the suppressed monsoon period and varied diurnally during the monsoon break. This pattern of variation is represented well in the model simulations. Figure 8 shows the variation of the observed (panel a) and simulated (panel b) temperature perturbations and cirrus cover.

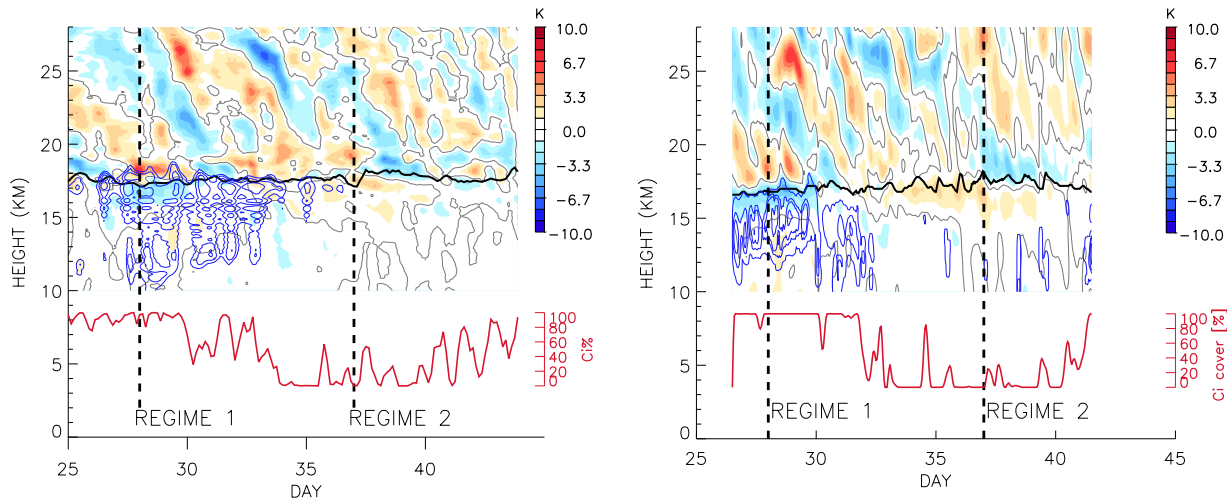


Figure 8. Time-height evolution of temperature perturbations (shaded) in observations (a) and simulations (b). Blue contours show the observed super-saturation over ice (a) and simulated ice content (in b). Red lines show the percentage of the area covered by cirrus within 150 km from Darwin. In panel a, cirrus cover is taken from the variational analysis dataset. In panel b, cirrus is defined as the presence of ice content. Black solid lines show the height of minimum temperature.

The operational radiosonde sounding showed ice supersaturation and oscillations in the wind and temperature field consistent with vertically propagating gravity waves. The simulations using the WRF produce supersaturation with respect to ice and wave features comparable to those observed.

## References

- Geller, M. A., and J. Gong, 2010. Gravity wave kinetic, potential, and vertical fluctuation energies as indicators of different frequency gravity waves, *J. Geophys. Res.*, **115**, D11,111, doi:10.1029/2009JD012,266
- Gong, J., and M. Geller, 2010. Vertical fluctuation energy in United States high vertical resolution radiosonde data as an indicator of convective gravity}, *J. Geophys. Res.*, **115**, D11,110, doi:10.1029/2009JD012,265.
- Lane, T. P., M. J. Reeder and F. M. Guest. 2003. Convectively-generated gravity waves observed from radiosonde data taken during MCTEX. *Quart. J. Roy. Meteor. Soc.* **129**, 1731 – 1740.
- Marks, C. J., and S. D. Eckermann, 1995. A three-dimensional nonhydrostatic ray-tracing model for gravity waves: Formulation and preliminary results for the middle atmosphere, *J. Atmos. Sci.*, **52**, 1959 – 1984.
- May, P. T., J. H. Mather, G. Vaughan, C. Jakob, G. M. McFarquhar, K. N. Bower, and G. G. Mace, 2008. The tropical warm pool international cloud experiment, *Bull. Amer. Meteorol. Soc.*, **89**, 629 – 645, doi:10.1175/BAMS-89-5-629
- Skamarock, W. C., J. B. Klemp, J. Dudhia, D. O. Gill, D. M. Barker, W. Wang, J. G. Powers, 2005. A Description of the Advanced Research WRF Version 2. *NCAR Tech Note, NCAR/TN-468+STR*, 88 pp. [Available from UCAR Communications, P.O. Box 3000, Boulder, CO 80307].
- Steiner, M., M. J. Smith, and R. Uijlenjoet, 2004. A microphysical interpretation of radar reflectivity-rain rate relationships, *J. Atmos. Sci.*, **61**, 1114 – 1131.
- Xie, S., T. Hume, C. Jakob, S. A. Klein, R. B. McCoy, and M. Zhang, 2010. Observed large-scale structures and diabatic heating and drying profiles during TWP-ICE, *J. Climate*, **23**, 57 -9, doi:10.1175/2009JCLI3071.1.

**1 Gravity Waves Generated by Convection during**  
**2 TWP-ICE. Part I: Inertia-Gravity Waves**

Mai C. N. Hankinson,<sup>1</sup> M. J. Reeder,<sup>1</sup> and T. P. Lane<sup>2</sup>

---

Mai C.N. Hankinson, School of Mathematical Sciences, Monash University, Wellington Road, Melbourne, Victoria 3800, AUSTRALIA. (Mai.C.Nguyen@monash.edu)

M. J. Reeder, School of Mathematical Sciences and ARC Centre for Excellence for Climate System Science, Monash University, Wellington Road, Melbourne, Victoria 3800, AUSTRALIA. (Michael.Reeder@monash.edu)

T. P. Lane, School of Earth Sciences and ARC Centre of Excellence for Climate System Science, The University of Melbourne, Victoria 3010, AUSTRALIA. (tplane@unimelb.edu.au)

<sup>1</sup>School of Mathematical Sciences,  
Monash University, Melbourne, Victoria,  
AUSTRALIA.

<sup>2</sup>School of Earth Sciences, The University  
of Melbourne, Victoria, AUSTRALIA.

**Abstract.**

Gravity waves are analyzed in radiosonde soundings taken during the TWP-ICE campaign. The properties of the inertia-gravity waves are analyzed in Part I, whereas Part II focuses on high-frequency gravity waves. Two groups of inertia-gravity waves are detected: group L (L stands for Long vertical wavelength) in the middle stratosphere during the suppressed monsoon period, and group S (S stands for Short vertical wavelength) in the lower stratosphere during the monsoon break period. Waves belonging to group L propagate to the south-east with a mean intrinsic period of 35 h, and have vertical and horizontal wavelengths of about 5-6 km and 3000-6000 km, respectively. Ray tracing calculations indicate that these waves originate from a deep convective region near Indonesia. Waves belonging to group S propagate to the south-south-east with an intrinsic period, vertical wavelength and horizontal wavelength of about 45 h, 2 km and 2000-4000 km, respectively. These waves are shown to be associated with shallow convection in the oceanic area within about 1000 km of Darwin.

19

## 1. Introduction

20 Gravity waves can transport momentum and energy large distances from the site of  
21 their generation, exerting a stress on the atmosphere as they dissipate. Although the  
22 effect of individual wave packets on the momentum budget of the atmosphere is small,  
23 the long term accumulated effects are important in climate [see, for example, the recent  
24 review by *Alexander et al.*, 2010].

25  
26 The present two-part study focuses on observations of convectively-generated gravity  
27 waves. A number of physical mechanisms have been identified as being important in  
28 the generation of gravity waves by convection. These mechanisms include: the temporal  
29 variations of the diabatic heating in the clouds [e.g. *Salby and Garcia*, 1987; *Bretherton*,  
30 1988; *Lin et al.*, 1998; *H.-Y and Baik*, 1998]; the blocking effects of the convective clouds  
31 in the vertically sheared environment [e.g. *Clark et al.*, 1986; *Hauf and Clark*, 1989; *Beres*  
32 *et al.*, 2002]; and the mechanical oscillator effect, in which the overshooting convective up-  
33 drafts encounter a stable layer aloft, decelerate quickly, and subsequently oscillate about  
34 their level of neutral buoyancy [*Pierce and Coroniti*, 1966; *Fovell et al.*, 1992; *Lane et al.*,  
35 2001]. These mechanisms have been evaluated in previous modeling studies [e.g. *Fovell*  
36 *et al.*, 1992; *Lane et al.*, 2001; *Lane and Reeder*, 2001a, b; *Beres et al.*, 2002; *Lane and*  
37 *Moncrieff*, 2008; *Grimsdell et al.*, 2010]. One of the problems in assessing the relative  
38 importance of these different mechanism is the lack of detailed observations.

39

40 Observational studies of convectively-generated waves have been based principally on  
41 radars [e.g. *Sato et al.*, 1995; *Dhaka et al.*, 2005], aircraft [e.g. *Alexander et al.*, 2000],  
42 satellites [e.g. *Hecht et al.*, 2009, using airglow imagery] and radiosondes [*Karoly et al.*,  
43 1996; *Lane et al.*, 2003; *Gong and Geller*, 2010; *Ki and Chun*, 2011]. The work described  
44 here is based mostly on radiosonde observations from the Tropical Warm Pool Interna-  
45 tional Cloud Experiment (TWP-ICE), which took place in Darwin, Australia (near 130°E,  
46 12°S) from 17 January to 13 February, 2006. (See Figure 1 for the location of TWPICE  
47 domain.) The campaign experiment is described in detail by *May et al.* [2008].

48  
49 There are many studies that have used the observations taken during TWP-ICE, in-  
50 cluding a few focused principally on gravity waves. Using radiosonde observations, *Evan*  
51 *and Alexander* [2008] identified inertia-gravity waves with periods of about 2 days during  
52 the suppressed monsoon period, which coincided with the end of the easterly phase of the  
53 quasi-biennial oscillation. These waves propagated to the south-east and had vertical and  
54 horizontal wavelengths around 6 km and 5500-7000 km respectively. *Evan et al.* [2012]  
55 extended this work using the European Centre for Medium-Range Weather Forecasts  
56 (ECMWF) operational analyses and the Weather Research and Forecasting model. Their  
57 simulation is consistent with the observations by [*Evan and Alexander*, 2008] and indicates  
58 that these waves originated from deep convection in the Indonesian region. Using satellite  
59 imagery, *Hecht et al.* [2009] found waves (during the suppressed monsoon period) at an  
60 altitude near 40 km with horizontal wavelengths between 200 and 400 km . Furthermore,  
61 *Hecht et al.* [2009] identified two groups of waves at 80 km altitude in air glow images  
62 taken in the Alice Spring area: the first group had periods of 1 to 2 hours whereas the

63 second group had periods of 15 to 25 minutes and horizontal wavelengths of 30 to 40 km.

64 This second group of waves were thought to have been generated by convection within a

65 mesoscale system located between Darwin and Alice Springs.

66  
67 The main goal of the present work is to deduce the properties of convectively-generated

68 gravity waves from the radiosonde observations made during TWP-ICE. This research

69 builds on past work by examining the TWP-ICE period and by analyzing the radiosonde

70 data for both inertia-gravity waves and high-frequency waves. The present paper is the

71 first of two. Here (Part I) the results on inertia-gravity waves are reported while in the

72 companion paper (Part II) the results on high-frequency waves are described. Gravity

73 waves have frequencies which lie between the inertial frequency  $f$  and the buoyancy fre-

74 quency  $N$ . When the effects of the rotation of the Earth are important, and hence, the

75 frequency lies closer to  $f$  than  $N$ , the waves are called inertia-gravity waves. In the present

76 study, the inertia-gravity waves analyzed have periods longer than about a day, and this

77 is adopted here as a practical definition of inertia-gravity waves. High-frequency gravity

78 waves are defined here as gravity waves for which the effects of the Earth's rotation can

79 be neglected. These waves, analyzed in Part II, have periods which are a few multiples of

80 the buoyancy period ( $2\pi/N$ ). Hence, there is a clear separation in time scales between the

81 inertia-gravity waves reported in Part I and the high-frequency waves reported in Part II.

82  
83 The remainder of this part is organized as follows. Descriptions of the observations and

84 data analysis are given in Section 2. The analyzed properties of the inertia-gravity waves

are reported in Section 3. Our conclusions are given in Section 4.

## 2. Data

The data to be analyzed are summarized now.

### 2.1. Profiles from the variational analysis during TWP-ICE

The profiles constructed by a variational analysis from the observations taken during the TWP-ICE campaign [Xie *et al.*, 2010] are used to define the mean state of the atmosphere. The variational analysis, which is an objective analysis method, follows the method developed by Zhang and Lin [1997] to derive profiles of large-scale variables from a small network of sounding stations. The essence of this variational analysis method is to make small perturbations to the observed profiles of temperature, wind and humidity while conserving column-integrated mass, moisture, energy, and momentum. The variational analysis is constrained by the domain-averaged surface and top-of-the-atmosphere observations (e.g., radiative and heat fluxes and precipitation). Initial analyses of temperature, wind and humidity are required for the variational analysis. These are generated from TWP-ICE soundings using the interpolation scheme described by Cressman [1959] with the background from the ECMWF analyses. The profiles from the variational analysis represent the time-evolving conditions averaged over a  $2\times 2$  degree box centered on the campaign area (see Fig. 1). As described more precisely below, inertia-gravity waves are identified with perturbations from this mean state.

104 Figure 2 shows time-height variation of the mean zonal and meridional wind ( $u$  and  
105  $v$ ) profiles from the variational analysis. Marked on the figure are the synoptic regimes  
106 identified by *May et al.* [2008]. In the stratosphere, the maximum easterly wind is about  
107  $35 \text{ m s}^{-1}$  near 24 km altitude (Fig. 2a) and the strongest wind shear, about  $2 \text{ m s}^{-1}$   
108  $\text{km}^{-1}$ , is in the 20-22 km layer. For the meridional wind component (Fig. 2b), during  
109 the suppressed monsoon period, there is a layer of relatively strong southerly wind near  
110 the top of the troposphere with a maximum of about  $18 \text{ m s}^{-1}$  at 15 km altitude. This  
111 layer is associated with the strong upper-level outflow from a large mesoscale convective  
112 system located at this time to the south-west of the TWP-ICE domain. Accordingly, the  
113 layer of strongest wind shear is located in the upper troposphere with maximum around  
114  $15 \text{ m s}^{-1} \text{ km}^{-1}$ . It will be shown in Section 3 that, in the stratosphere, the effects of the  
115 vertical wind shear on the properties of the inertia-gravity waves are small for the current  
116 study.

117

## 2.2. Radiosonde soundings

118 The radiosonde soundings from five stations (Cape Don, Darwin, Garden Point, Mount  
119 Bundy and Point Stuart) are the main data used here. The vertical soundings of wind  
120 speed and direction, air temperature, mixing ratio, pressure and the altitude of the balloon  
121 are available every 3 hours with the time resolution of 2 seconds (except for Darwin where  
122 the soundings are only available every 6 hours). Perturbations of the vertical motion  $w$   
123 are used for high-frequency gravity waves and will be presented in Part II of the paper.  
124 For this study, the profiles of wind components ( $u$  and  $v$ ), temperature  $T$ , mixing ratio  $q$   
125 and pressure  $p$  are interpolated to a regular grid of 15 m resolution to a height of 30 km.

126 Since perturbations in the troposphere contain signals from processes other than gravity  
127 waves such as turbulence and convection, the analysis of the gravity waves is carried out  
128 in the stratosphere from 17.5 to 28 km (the tropopause is located near 17 km during the  
129 campaign).

130

131 Quality control of the observed soundings was carried out by eliminating values differing  
132 by more than 3 standard deviations from the mean of all stations at the same height and  
133 time. In addition, profiles extending less than 1.5 km above the tropopause are not used  
134 in the analysis in the stratosphere. During the period from 21 January to 13 February  
135 2006, about 75% of soundings reach the stratosphere while about 60% of total soundings  
136 reaching 28 km. Missing observations of  $u$ ,  $v$ ,  $p$ ,  $T$  are filled by treating the data at a  
137 given station and height as a time series and then linearly interpolating in time. Although  
138 filling these missing data is not needed for the quality control, it is necessary for the later  
139 frequency spectral analysis.

140

141 The perturbations of  $u$ ,  $v$  and  $T$ , hereafter denoted as  $u'$ ,  $v'$  and  $T'$ , respectively, are cal-  
142 culated by assuming the profiles constructed by variational analysis as the mean profiles.  
143 The basic assumption underpinning the analysis is that these perturbations physically  
144 represent inertia-gravity waves. Two additional methods of defining the mean state are  
145 tested to access the sensitivity of the results to the choice of mean state. In the first  
146 method, which is similar to that used by *Evan and Alexander* [2008], the mean state of  
147 each station at each height is defined as the linear trend of the time series of the obser-  
148 vations for the corresponding height and station. In the second method, the mean state

149 is defined by a polynomial fitted to each vertical profile using least squares. The different  
150 mean states gave similar patterns of perturbations, although their magnitudes could be  
151 different by as much as a few  $\text{m s}^{-1}$ . The use of variational analysis as the background  
152 state has advantages. First, profiles from the variational analysis represent a physically  
153 evolving large-scale environment rather than an arbitrary mean state commonly used by  
154 other methods. Second, using the variational analysis effectively removes the uncertain-  
155 ties associated with the arbitrary choice of the background, which were shown by *Zhang*  
156 *et al.* [2004] to cause significant uncertainties in the wave parameters analyzed by the  
157 hodograph method.

158  
159 Figure 3 shows the time-height evolution of the horizontal wind perturbations at Point  
160 Stuart. The evolution of the temperature perturbations (not shown) is similar to that of  
161 zonal wind with an amplitude of about 10 K. In Fig. 3, the phase propagation of  $u'$  and  
162  $v'$  is downward (marked by arrows), which is one of the properties of upward propagating  
163 gravity waves [e.g. *Andrews et al.*, 1987]. Figure 3 appears to show two distinct regimes  
164 with different phase speeds (given by the slope of the phase lines). The gravity waves in  
165 each regime will be analyzed separately. Note, these wave regimes are different from the  
166 meteorological regimes marked in Fig. 2.

167  
168 In the first regime (Regime 1, 28 January - 6 February), large amplitude perturbations  
169 (around  $8 - 20 \text{ m s}^{-1}$ ) with clearly descending phase propagation are evident in the 22-28  
170 km altitude range. The perturbations during this regime appear to be consistent with  
171 the 2-day inertia-gravity wave identified by *Evan and Alexander* [2008]. Waves in this

172 regime are referred to as group L hereafter (where L stands for Long vertical wavelength).  
173 This regime sits in the later part of the suppressed monsoon and the clear day periods  
174 identified by *May et al.* [2008].

175

176 The second regime (Regime 2, 7 - 13 February) coincides with the monsoon break pe-  
177 riod identified by *May et al.* [2008]. In this regime the downward phase propagation is  
178 most clearly evident below the heights of 22 km. Compared with the wave properties in  
179 Regime 1, these perturbations have lower downward phase speeds and smaller vertical  
180 wavelengths. Waves of this group are hereafter referred to as group S (where S stands for  
181 Short vertical wavelength). Although there are similar descending phase perturbations in  
182 the lower stratosphere during Regime 1, they are dominated by the signals at the higher  
183 altitudes.

184

### 2.3. Convective activity estimated from satellite

185 Infra-red measurements from the MTSAT satellite are used to estimate the convective  
186 activity. Convection is identified by the method following that of *Inoue* [1987]. Deep  
187 convection is assumed where brightness temperatures of the IR1 channel (10.3-11.3  $\mu\text{m}$ )  
188 is lower than a threshold value  $\text{IR1}_{top}$ , which signifies that the cloud top is above the  
189 middle troposphere, and the difference between channels IR1 and IR2 (11.5-12.5  $\mu\text{m}$ )  
190 is less than  $0.5^\circ\text{C}$ .  $\text{IR1}_{top}$  is chosen to be  $-10^\circ\text{C}$  which is above the 500 hPa level for the  
191 TWPICE data. Shallow convection is identified when brightness temperatures on channel  
192 IR1 is between  $\text{IR1}_{top}$  and  $2^\circ\text{C}$  and the (IR1-IR2) difference in the brightness temperature

193 is less than  $1^{\circ}\text{C}$ . The estimates of convective activity are used to study the tropospheric  
194 sources the gravity waves.

### 3. Inertia-Gravity Waves

195 The theory for linear, plane, gravity waves in a uniform environment shows that, given  
196 the amplitude of the horizontal component of the velocity perturbation, the amplitude of  
197 the vertical component of velocity increases with decreasing vertical wave number and in-  
198 creases with increasing horizontal wave number [e.g. see *Lane et al.*, 2003]. Consequently,  
199 measurements of the horizontal velocity perturbations and vertical velocity emphasize dif-  
200 ferent parts of the wave spectrum depending on the magnitudes of horizontal and vertical  
201 wavenumbers. Radiosonde measurements of the horizontal perturbation kinetic energy  
202  $\frac{1}{2}(u'^2 + v'^2)$  per unit mass emphasize the (low-frequency) inertia-gravity waves [*Geller and*  
203 *Gong*, 2010], whereas the vertical counterpart  $\frac{1}{2}w'^2$  emphasizes the high-frequency gravity  
204 waves. Accordingly, the properties of the inertia-gravity waves, which will be examined in  
205 this section, are extracted from the perturbations in horizontal wind components, whereas  
206 the high-frequency gravity waves, discussed in Part II, are extracted from the vertical wind  
207 perturbations.

208  
209 Figure 4 shows the ground-based frequency-vertical wavenumber quadrature power spec-  
210 tra (averaged over all stations) for the horizontal wind perturbations during Regimes 1  
211 and 2. The quadrature spectra are defined using Fourier analysis as the imaginary part  
212 of cross spectrum of the two horizontal components of the velocity. These quadrature  
213 spectra are calculated from the Fourier transform of the horizontal wind perturbations in  
214 the complex form  $(u' + iv')$ . The radiosondes used to construct Fig. 4 were launched every

215 3 hours. The quadrature spectra during the two regimes show clear differences. During  
216 Regime 1, the quadrature spectrum for waves of group L peaks at a ground-based period  
217 of 2.28 days and vertical wavelength of 5.2 km (left panel). During Regime 2, waves of  
218 group S have a ground-based period near 3.5 days and the vertical wavelengths in the  
219 range of 1.5 to 2.1 km (right panel). The properties of waves of groups L and S noted  
220 above are consistent with the phase lines marked by the arrows in Fig. 3. In addition,  
221 the perturbation plots (Fig. 3) show that, although group S has similar power in both  
222 Regimes 1 and 2, it does not appear clearly in the spectrum during Regime 1 (Fig. 4a)  
223 because the spectrum is dominated by group L (note, the amplitude scales in (a) and (b)  
224 are different). Consequently, group L will be analysed using data in the 22-28 km layer  
225 during Regime 1, whereas group S will be analysed using data in the 17.5-22 km layer  
226 during both regimes.

227

228 The process by which the frequency and horizontal and vertical wave numbers of the  
229 inertia-gravity waves are identified in the radiosonde soundings is as follows. First, the  
230 perturbations of the horizontal wind components and temperature are filtered (using  
231 a Fourier transform) to retain the frequencies with the peak powers indicated by the  
232 frequency-vertical wavenumber spectral analysis. For waves of groups L and S, the band-  
233 pass windows are between 1.7 and 3.3 days and 2.3 to 3.6 days, respectively. Second,  
234 the spectral Stokes parameter method developed by *Eckermann and Vincent* [1989] is  
235 used to determine the polarization ellipses (Section 3.1). A brief description of the Stokes  
236 parameter method is included in Appendix A.

237

238 There is no clear distinction between equatorially-trapped mixed Rossby-gravity and  
 239 freely propagating inertia-gravity waves. As will be shown in Section 3.1, both groups  
 240 L and S propagate to the south-east, which is different from the east-west propagation  
 241 direction predicted for mixed Rossby-gravity waves. Therefore, they will be treated as  
 242 inertia-gravity waves, which is the normal approach taken by similar studies. Wave prop-  
 243 erties of groups L and S are deduced from dispersion relation for inertia-gravity waves in  
 244 Section 3.2.

### 3.1. Polarization ellipses from the Stokes parameter method

246 Table 1 lists the properties of the polarization ellipses determined by the Stokes param-  
 247 eter method and the derived properties of groups L and S. Based on the power spectrum  
 248 shown in Fig. 4, group L is evaluated using one vertical wavenumber corresponding to  
 249 the wavelength of 5.2 km, whereas group S is evaluated using the vertical wavenumber  
 250 band corresponding to the wavelength range from 1.5 to 2.1 km (see Eq. A2 in Appendix  
 251 A). The polarization ellipses are illustrated in Fig. 5. The angle  $\Theta$  between the major  
 252 axis of the polarization ellipse and the eastward horizontal axis indicates the direction  
 253 of the horizontal number wave vector with the ambiguity of 180 degrees. The horizontal  
 254 wave propagation direction is calculated also using the method described by *Vincent et al.*  
 255 [1997] and *Evan and Alexander* [2008], which does not suffer this ambiguity. In this case,  
 256 the direction in which the wave propagates is

$$\Theta_{T'_{+90}} = \tan^{-1} \left( \frac{\overline{u'T'_{+90}}}{\overline{v'T'_{+90}}} \right) \quad (1)$$

257

258 where  $\Theta_{T'_{+90}}$  is the angle between the wave propagation direction and the eastward hori-  
 259 zontal axis and  $T'_{+90}$  is the value of the temperature perturbation after shifting the phase  
 260 by  $+90^\circ$  using a Hilbert transform. Although mixed Rossby-gravity waves also have  
 261 hodographs which rotate anticyclonically with height, their major axis should be east-  
 262 west (see Appendix B).

263

264 For waves of group L, the mean horizontal wave direction  $\Theta$  estimated by the orienta-  
 265 tion of the polarization ellipses is  $-40.2$  degrees, i.e. towards the south-east, with standard  
 266 deviation of  $12.8$  degrees. Using Eq. 1 gives a similar direction,  $-51.3$  degrees on average,  
 267 with standard deviation of  $7.8$ . The degree of polarization  $d$  is high ( $0.96$  on average)  
 268 indicating that the signal is dominated by coherent waves rather than noise. The ratio  
 269 of the minor to major axes of the ellipse  $r$ , which is related to the ratio of the inertial  
 270 frequency  $f$  to the intrinsic frequency of the waves  $\omega_*$  (see Eq. 3 in Section 3.2), has a  
 271 mean of  $0.63$  and standard deviation of  $0.12$ .

272

273 The waves comprising group S are less polarized than group L, with  $d = 0.74$  (on  
 274 average). The propagation direction is more southward (see Fig. 5a and b), with the  
 275 averages of  $\Theta$  and  $\Theta_{(T'_{+90})}$  being  $-72.2$  and  $-66.0$  degrees, respectively. For these waves, the  
 276 standard deviation (among the stations) of the propagation direction  $\Theta$  is relatively large  
 277 ( $25.4$  degrees), whereas  $\Theta_{(T'_{+90})}$  has a much smaller standard deviation ( $3.4$  degrees). The  
 278 polarization ellipses for waves of group S have relatively large ratios  $r$  ( $0.82$  on average),

279 indicating that the intrinsic frequencies are low.

280  
281 Following *Eckermann* [1996], the Stokes parameters are used to also determine the ver-  
282 tical direction of energy propagation (see Eq. A4 in Appendix A). The ratios of the  
283 upward and downward energy propagation for each group are shown in Table 1. Both  
284 groups L and S have upward energy propagation as these ratios are much greater than 1,  
285 the averages being 15.6 and 6.6, respectively.

### 3.2. Estimation of inertia-gravity wave properties

When the effects of a linear vertical wind shear and the variation of density with height are taken into account, the dispersion relation of inertia-gravity waves is

$$\omega_*^2 = f^2 + \frac{N^2 k_h^2}{m^2 + 1/(4H_s^2)} - \frac{2fk_h m \overline{V_z}}{m^2 + 1/(4H_s^2)} \quad (2)$$

287 where  $H_s = \rho/\rho_z$  is the density scale height,  $k_h = |\underline{K}|$  is the magnitude of horizontal wave  
288 vector  $\underline{K}$ ,  $m$  is the vertical wavenumber,  $\overline{V_z}$  is mean vertical wind shear in the direction  
289 perpendicular to the direction of wave propagation. The overbar denotes averaging in  
290 both time and height. In Eq. 2, the coordinate system is aligned in such a way that the  
291 x-axis is parallel to the wavenumber vector.

292  
For inertia-gravity waves, the horizontal wind perturbation vectors rotate with height and their hodographs describe polarization ellipses with the major axis parallel to the

wavenumber vector. The ratio of minor axis to the major axis  $r$  is

$$r = \frac{f}{\omega_*} - \frac{k_h m \overline{V_z}}{[m^2 + 1/(4H_s^2)] \omega}. \quad (3)$$

Equations 2 and 3 are then used to form the equation for  $\omega_*$ :

$$\omega_*^2(r^2 - a^2) - 2\omega_* f r(1 - a^2) + f^2(1 - a^2) = 0 \quad (4)$$

where  $a^2 = \frac{V_z^2}{N^2[1+(4m^2H_s^2)^{-1}]}$ . As shown by *Hines* [1989], the background wind shear may induce an additional ellipticity to the vertical profiles of horizontal wind perturbations, making quasi-stationary gravity waves to appear to have longer periods. Thus, the intrinsic period  $\omega_*$  is taken as the root of Eq. 4 corresponding to the larger frequency (shorter periods), in which case

$$\frac{\omega_*}{f} = \frac{r(1 - a^2) + [r^2(1 - a^2)^2 - (r^2 - a^2)(1 - a^2)]^{1/2}}{r^2 - a^2}. \quad (5)$$

Given  $\omega_*$  and  $m$ , the dispersion relation (Eq. 2) can be rearranged to give the horizontal wavenumber, in which case

$$k_{disp} = \frac{f m \overline{V_z}}{N^2} \pm \frac{1}{N} \left[ \frac{f^2 m^2}{N^2} \overline{V_z}^2 + (\omega_*^2 - f^2) \left( m^2 + \frac{1}{4H_s^2} \right) \right]^{1/2} \quad (6)$$

293

294 where  $k_{disp}$  takes the positive values in the wave propagation direction, which was esti-  
 295 mated earlier by the Stokes parameter method. Note that as  $H_s \rightarrow \infty$  Eqs. 2, 5 and 6  
 296 reduce to Eqs. 3, 5 and 6 in *Cho* [1995].

297

Alternatively, the horizontal wavenumber can be deduced from the difference between the observed ground-based frequency  $\omega$  and the intrinsic frequency  $\omega_*$  using the expression for doppler shifting

$$k_{dopp} = \frac{\omega - \omega_*}{\bar{U}}. \quad (7)$$

Here  $\bar{U}$  is the mean horizontal wind component in the direction of wave propagation.

The wave properties calculated using Eqs. 5-7 are listed in Table 1. The intrinsic period of group L ranges from 27 to 43 hours with an average of 35.2 for all the stations. This mean intrinsic period is shorter than that of group S, which is 45 hours. The inertial period at Darwin is 57.6 hours. The mean horizontal wavelengths calculated using the doppler relation (Eq. 7) are 5300 km and 4000 km for groups L and S, respectively. The estimate for the horizontal wavelength of group L is similar to the 2-day inertia gravity wave found by *Evan and Alexander* [2008], who used the phase lag between stations to determine the horizontal wavelength. *Evan and Alexander* [2008] calculated the vertical wavelength of these waves to be about 6 km, the horizontal wavelength to be around 5500 to 8700 km, and the propagation direction to be to the south-east. Inertia-gravity waves with similar properties to those of group S have been found to be common in the lower stratosphere by previous authors [*Thompson, 1978; Sato, 1994; Wada et al., 1999*].

As a check on the consistency between the results presented here and those from *Evan and Alexander* [2008], the horizontal wavelengths are also calculated from the dispersion

319 relation (using Eq. 6). In this case, the horizontal wavelengths are smaller with the  
320 average values of 3300 km and 2100 km for groups L and S respectively. Although the  
321 same order of magnitude, the horizontal wavelengths calculated using Eqs. 6 and 7 are  
322 different. This difference arises from the inclusion of vertical wind shear in Eq. 6, as  
323 well as the uncertainties in estimating vertical wavenumber  $m$  in Eq. 6 and ground-based  
324 frequency  $\omega$  in Eq. 7 from discrete spectral analysis. Of these, the uncertainties in  $m$   
325 and  $\omega$  explain most of the difference; at low wavenumbers the uncertainty can be as large  
326 as 100%. The effects of the vertical wind shear on the estimates of wave properties are  
327 relatively small (less than 2%) for group L (with  $\overline{V_z} \approx -0.5 \text{ m s}^{-1} \text{ km}^{-1}$ ). In the layer  
328 below 22 km, where the mean vertical wind shear is around  $2 \text{ m s}^{-1} \text{ km}^{-1}$ , the effects of  
329 the vertical wind shear on group S are larger (5% for  $\omega$  and 16% for  $k$ ). Although  $H_s$  ( $\approx$   
330 6 km) is comparable to  $\lambda_z$  ( $\approx 5.2 \text{ km}$ ), taking the limit as  $H_s \rightarrow \infty$  in Eqs. 2 and 3 only  
331 affects the result by less than 0.05%.

332

### 3.3. Ray tracing

333 Wave groups L and S are further investigated by backward ray-tracing to understand  
334 their origins and association with convective sources. For this purpose, the program suite  
335 GROGRAT, which is developed and described by *Marks and Eckermann* [1995], is em-  
336 ployed using wind and temperature fields from the 6-hourly ERA Interim reanalysis<sup>1</sup>.  
337 The properties of the waves are taken from Table 1. The type of convection along each  
338 ray is identified following the method of *Inoue* [1987] using hourly infrared satellite data  
339 from MTSAT (see Section 2.3). The presence of convection in each section between two  
340 consecutive points along the ray is defined if the area covered by convection is at least

341 10% in a  $1^\circ \times 1^\circ$  box centered at the middle of the section. In the case of long sections,  
342 the box is expanded to fit the whole section.

343  
344 Figure 6 shows rays of groups L and S traced backward from 00Z 04 February and 00Z  
345 08 February 2006, respectively. Rays in group L originate mainly from the area 123E-127E  
346 and 7S-0.5S (panel a) near Indonesia where deep convection is analyzed. While passing  
347 this deep convection region, the rays are in the middle troposphere from 3-17 km (panel  
348 c). Thus, it appears that these waves were generated by deep convection in this region.  
349 Waves in group S, as shown in panels b and d, propagate from an arc of about 1000 km  
350 radius to the north of the TWPICE domain. These rays primarily pass over oceanic areas  
351 and are associated with shallow convection.

#### 4. Conclusions

353 Radiosonde observations from the TWP-ICE campaign were analyzed for inertia-gravity  
354 waves. The profiles obtained by variational analysis, which represents a physically evol-  
355 ving large-scale environment, are used to define the background fields. This approach  
356 removes the arbitrary choices for the background state common in other methods. Two  
357 wave groups, L and S, were found during the suppressed monsoon and monsoon break  
358 periods of TWPICE. Waves of group L, found during the suppressed monsoon period in  
359 the middle stratosphere, had properties consistent with the 2-day inertia-gravity waves  
360 described by *Evan and Alexander* [2008]. Their vertical wavelengths were about 6 km,  
361 their horizontal wavelengths were of order of 3000 - 6000 km, and their intrinsic periods  
362 ranged from 27 to 43 h with a mean of 35.2 h. During the monsoon break period, waves

363 of group S were detected in the lower layer of the stratosphere (in the 17.5-22 km layer)  
 364 with an intrinsic period near 45 hours. These waves had vertical wavelengths of 2 - 4 km,  
 365 horizontal wavelengths of 2000-4000 km, and intrinsic periods near 45 hours. The hori-  
 366 zontal propagation direction was from north-north-west and the vertical group velocity is  
 367 upward, indicating the energy source of these waves is in the troposphere.

368  
 369 Backward ray tracing was employed to identify the potential sources of the groups.  
 370 Waves in group L were associated with a region of deep convection in Indonesia. Waves  
 371 in group S were traced to the oceanic regions surrounding Darwin. Shallow convection,  
 372 found along the rays in group S, was the most likely source of these waves. It was shown  
 373 that the sources of inertia gravity waves observed over Darwin originated from convec-  
 374 tion  $\sim 1000$  km away. In Part II, the high-frequency waves detected in the soundings will  
 375 be shown to be generated locally from convection in the TWP-ICE domain and its vicinity.

### Appendix A: Stokes parameter method

377 Stokes parameters are calculated using the formulation of *Eckermann and Vincent*  
 378 [1989]. These parameters are

$$\begin{aligned}
 \tilde{I}(m) &= A(\overline{U_R^2(m)} + \overline{U_I^2(m)} + \overline{V_R^2(m)} + \overline{V_I^2(m)}) \\
 \tilde{D}(m) &= A(\overline{U_R^2(m)} + \overline{U_I^2(m)} - \overline{V_R^2(m)} - \overline{V_I^2(m)}) \\
 \tilde{P}(m) &= 2A(\overline{U_R(m)V_R(m)} + \overline{U_I(m)V_I(m)}) \\
 \tilde{Q}(m) &= 2A(\overline{U_R(m)V_I(m)} - \overline{U_I(m)V_R(m)})
 \end{aligned}
 \tag{A1}$$

379  
 380 where  $m$  is the vertical wavenumber,  $A$  is a constant, and the subscripts  $R$  and  $I$  denote

381 the real and imaginary parts of the Fourier transforms of the vertical perturbation profiles  
 382 of  $u'$  and  $v'$ . The overbars denote the average of all profiles available during each regime.  
 383 The Stokes parameters are evaluated for a given vertical wavenumber band by integrating  
 384 in wavenumber space according to the expression

$$X_{m_1, m_2} = \int_{m_1}^{m_2} \tilde{X}(m) dm \quad (\text{A2})$$

385  
 386 where  $X_{m_1, m_2}$  is one of the Stokes parameters in (A1) evaluated over a wavenumber band  
 387 between  $m_1$  and  $m_2$ .

388 The properties of the polarization ellipses are then evaluated as

$$\begin{aligned} d &= \frac{(D^2 + P^2 + Q^2)^{1/2}}{I} \\ \Theta &= \frac{1}{2} \tan^{-1} \left( \frac{P}{D} \right) \\ \delta &= \frac{1}{2} \tan^{-1} \left( \frac{Q}{P} \right) \\ R &= \tan \left[ \frac{1}{2} \sin^{-1} \left( \frac{Q}{dI} \right) \right] \end{aligned} \quad (\text{A3})$$

389  
 390 where  $d$  is the degree of polarization,  $\Theta$  is the angle of the major axis counter-clockwise  
 391 from the eastward direction;  $\delta$  is the phase difference between  $u'$  and  $v'$  components, and  
 392  $R$  is the ratio between the major to the minor axes of the ellipse.

393  
 394 Following *Eckermann* [1996], clockwise (CW) and anticlockwise (ACW) rotation of the  
 395 horizontal wind perturbations with height can be determined from Stokes parameters as  
 396 follows

$$\begin{aligned}
 \tilde{C}W(m) &= 0.5 \left[ \tilde{I}(m) - \tilde{Q}(m) \right] \\
 A\tilde{C}W(m) &= 0.5 \left[ \tilde{I}(m) + \tilde{Q}(m) \right].
 \end{aligned}
 \tag{A4}$$

397

398

## Appendix B: Hodograph rotation for Mixed Rossby-Gravity waves

399 Following *Andrews et al.* [1987] consider the Boussinesq equations on an equatorial beta  
 400 plane linearized about a basic state at rest and with constant Brunt-Vaisala frequency  $N$ .  
 401 The solution the horizontal velocity in a Mixed Rossby-Gravity wave is

$$(u', v') = \hat{v}_0 \omega y \exp\left(\frac{-\beta|m|y^2}{2N}\right) \cos(mz) \left(-\frac{|m|}{N} \sin(kx - \omega t), \cos(kx - \omega t)\right) \tag{B1}$$

with dispersion relation

$$m = -\text{sgn}(\omega)(\beta + \omega k) \frac{N}{\omega^2}. \tag{B2}$$

Then

$$u'^2 + \left(\frac{m\omega y}{N}\right)^2 v'^2 = \left(\frac{\hat{v}_0 m \omega y}{N} \cos(mz)\right)^2 \exp\left(\frac{-\beta|m|y^2}{N}\right) \tag{B3}$$

402

403 which describes an ellipse aligned along the x-axis (the zonal direction) with the ratio of  
 404 the minor to major axes is  $r = (N/m\omega y)$  (provided  $y \neq 0$ ), from which  $\omega = N/(mry)$ .

405

The angle with the x-axis made by the horizontal wind vector  $(u', v')$  is  $\tan \Theta = -\cot(kx - \omega t)/(|m|\omega y)$ , and hence

$$\frac{\partial \Theta}{\partial z} = -\frac{1}{|\omega|y} \left( \frac{N^2(\beta + \omega k)}{|m| \sin^2(kx - \omega t)} \right). \quad (\text{B4})$$

406

In the Northern (Southern) Hemisphere,  $y > 0$  ( $y < 0$ ) and  $\Theta$  decreases (increases) as  $z$  increases, meaning that  $\Theta$  rotates anticyclonically (in both hemispheres).

409

**Acknowledgments.** This research was supported by the Office of Science (BER), US Department of Energy. Todd Lane is supported by an Australian Research Council Future Fellowship (FT0990892). We would like to thank the three anonymous reviewers for their thoughtful comments and suggestions which helped to improve the manuscript greatly.

414

## Notes

1. Additional ray-tracing tests are performed with the ERAI data averaged over the periods of Regimes 1 and 2 in order to remove the long-period waves from the mean environment. The results are similar to the case with 6-hourly data and are not shown here for brevity.

415

## References

- Alexander, M. J., J. H. Beres, and L. Pfister, Tropical stratospheric gravity wave activity and relationships to clouds, *J. Geophys. Res.*, *105*, 22,299–22,309, 2000.
- Alexander, M. J., et al., Recent developments in gravity-wave effects in climate models and the global distribution of gravity-wave momentum flux from observations and models, *Quart. J. Roy. Meteorol. Soc.*, *136*, 1103–1124, 2010.

420

- 421 Andrews, D., J. R. Holton, and C. B. Leovy, *Middle Atmosphere Dynamics*, pp 429 pp.,  
422 Academic Press, 1987.
- 423 Beres, J. H., M. J. Alexander, and J. Holton, Effects of tropospheric wind shear on the  
424 spectrum of convectively generated gravity waves, *J. Atmos. Sci.*, *59*, 1805–1824, 2002.
- 425 Bretherton, C. S., Group velocity and the linear response of stratified fluids to internal  
426 heat or mass sources, *J. Atmos. Sci.*, *45*, 81–93, 1988.
- 427 Cho, J. Y. N., Inertio-gravity wave parameter estimation from cross-spectral analysis, *J.*  
428 *Geophys. Res.*, *100(D9)*, 727–18, 1995.
- 429 Clark, T. L., T. Hauf, and J. P. Kuettner, Convectively forced internal gravity waves:  
430 Results from two-dimensional numerical experiments, *Quart. J. Roy. Meteorol. Soc.*,  
431 *112*, 899–925, 1986.
- 432 Cressman, G., An operational objective analysis scheme, *Mon. Weather Rev.*, *87*, 367–374,  
433 1959.
- 434 Dhaka, S. K., M. K. Yamamoto, Y. Shibagaki, H. Hashiguchi, M. Yamamoto,  
435 and S. Fukao, Convection-induced gravity waves observed by the equatorial at-  
436 mosphere radar (0.2°S, 100.32°E) in Indonesia, *Geophys. Res. Lett.*, *32*, L14,820,  
437 doi:10.1029/2005GL022,907.2, 2005.
- 438 Eckermann, S. D., Hodographic analysis of gravity waves: relationships among Stokes  
439 parameters, rotary spectra and cross-spectral methods, *J. Geophys. Res.*, *101*, 169–19,  
440 1996.
- 441 Eckermann, S. D., and R. A. Vincent, Falling sphere observations of anisotropic gravity  
442 wave motions in the upper stratosphere over Australia, *Pure and Applied Geophysics*  
443 *PAGEOPH*, *130*, 509–532, 1989.

444 Evan, S., and M. J. Alexander, Intermediate-scale tropical Inertia gravity waves  
445 observed during the TWP-ICE campaign, *J. Geophys. Res.*, *113*, D14,101,  
446 doi:10.1029/2007JD009,289, 2008.

447 Evan, S., M. J. Alexander, and J. Dudhia, Model study of intermediate-scale tropical  
448 inertia-gravity waves in comparison to TWP-ICE campaign observations, *J. Atmos.*  
449 *Sci.*, *69*, 591–610, 2012.

450 Fovell, F., D. Durran, and J. R. Holton, Numerical simulation of convectively generated  
451 stratospheric gravity waves, *J. Atmos. Sci.*, *49*, 1427–1442, 1992.

452 Geller, M. A., and J. Gong, Gravity wave kinetic, potential, and vertical fluctuation  
453 energies as indicators of different frequency gravity waves, *J. Geophys. Res.*, *115*,  
454 D11,111,doi:10.1029/2009JD012,266, 2010.

455 Gong, J., and M. Geller, Vertical fluctuation energy in United States high vertical res-  
456 olution radiosonde data as an indicator of convective gravity, *J. Geophys. Res.*, *115*,  
457 D11,110,doi:10.1029/2009JD012,265, 2010.

458 Grimsdell, A., M. J. Alexander, P. T. May, and L. Hoffmann, Model study of waves  
459 generated by convection with direct validation via satellite, *J. Atmos. Sci.*, *67*, 1617–  
460 1631, 2010.

461 H.-Y, C., and J.-J. Baik, Momentum flux by thermally induced internal gravity waves  
462 and its approximation for large-scale models, *J. Atmos. Sci.*, *55*, 3299–3310, 1998.

463 Hauf, T., and T. Clark, Three-dimensional numerical experiments on convectively forced  
464 internal gravity waves, *Quart. J. Roy. Meteorol. Soc.*, *115*, 309–333, 1989.

465 Hecht, J., et al., Imaging of atmospheric gravity waves in the stratosphere and upper  
466 mesosphere using satellite and ground-based observations over Australia during the

- 467 TWPICE campaign, *J. Geophys. Res.*, *114*, D18,123,doi:10.1029/2008JD011,259, 2009.
- 468 Hines, C. O., Tropopausal mountain waves over Arcibo: a case study, *J. Atmos. Sci.*, *46*,  
469 476–488, 1989.
- 470 Inoue, T., A cloud type classification with NOAA 7 Split-window measurements, *J. Geo-*  
471 *phys. Res.*, *92*, 3991–4000, 1987.
- 472 Karoly, D. J., G. L. Roff, and M. J. Reeder, Gravity waves activity associated with tropical  
473 convection detected in TOGA COARE sounding data, *Geophys. Res. Lett.*, *23*, 261–264,  
474 1996.
- 475 Ki, M.-O., and H.-Y. Chun, Inertia gravity waves associated with deep convection observed  
476 during the summers of 2005 and 2007 in Korea, *J. Geophys. Res.*, *116*, D16,122, 2011.
- 477 Lane, T. P., and M. W. Moncrieff, Stratospheric gravity waves generated by multiscale  
478 tropical convection., *J. Atmos. Sci.*, *65*, 2598–2614, 2008.
- 479 Lane, T. P., and M. J. Reeder, Convectively generated gravity waves and their effect on  
480 the cloud environment, *J. Atmos. Sci.*, *58*, 2427–2440, 2001a.
- 481 Lane, T. P., and M. J. Reeder, Modelling the generation of gravity waves by a maritime  
482 continent thunderstorm, *Quart. J. Roy. Meteorol. Soc.*, *127*, 2705–2724, 2001b.
- 483 Lane, T. P., M. J. Reeder, and T. L. Clark, Numerical modeling of gravity waves genera-  
484 tion by deep tropical convection, *J. Atmos. Sci.*, *58*, 1249–1274, 2001.
- 485 Lane, T. P., M. J. Reeder, and F. M. Guest, Convectively generated gravity waves ob-  
486 served from radiosonde data taken during MCTEX, *Quart. J. Roy. Meteorol. Soc.*, *129*,  
487 D11,111, doi:10.1029/2009JD012,266, 2003.
- 488 Lin, Y.-L., R. L. Deal, and M. S. Kulie, Mechanisms of cell regeneration, development, and  
489 propagation within a two-dimensional multicell storm, *J. Atmos. Sci.*, *55*, 1867–1886,

490 1998.

491 Marks, C. J., and S. D. Eckermann, A three-dimensional nonhydro-dynamic ray-tracing  
492 model for gravity waves: formulation and preliminary results for the middle atmosphere,

493 *J. Atmos. Sci.*, *52*, 1959–1984, 1995.

494 May, P. T., J. H. Mather, G. Vaughan, C. Jakob, G. M. McFarquhar, K. N. Bower,  
495 and G. G. Mace, The tropical warm pool international cloud experiment, *Bull. Amer.*

496 *Meteorol. Soc.*, *89*, 629–645, doi:10.1175/BAMS-89-5-629, 2008.

497 Pierce, A. D., and S. C. Coroniti, A mechanism for the generation of acoustic-gravity  
498 waves during thunderstorm formation., *Nature*, *210*, 1209–1210, 1966.

499 Salby, M., and R. Garcia, Transient response to localized episodic heating in the tropics.

500 Part I: Excitation and short-time near-field behavior, *J. Atmos. Sci.*, *44*, 458–498, 1987.

501 Sato, K., A statistical study of the structure, saturation and sources of inertio-gravity  
502 waves in the lower stratosphere observed with the MU radar, *J. of Atmospheric and*

503 *Solar-Terrestrial Physics*, *56*, 755–774, 1994.

504 Sato, K., H. Hashiguchi, and S. Fukao, Gravity waves and turbulence associated with  
505 cumulus convection observed with the UHF/VHF clear-air doppler radars, *J. Geophys.*

506 *Res.*, *100*, 7111–7119, 1995.

507 Thompson, R. O. R. Y., Observation of inertial waves in the stratosphere, *Quart. J. Roy.*  
508 *Meteorol. Soc.*, *104*, 691–698, 1978.

509 Vincent, R. A., S. J. Allen, and S. D. Eckermann, Gravity-wave parameters in the lower  
510 stratosphere, in *Gravity wave processes: Their parameterization in global climate mod-*

511 *els*, edited by K. Hamilton, pp. 7–25, Springer, New York, 1997.

512 Wada, K., T. Nitta, and K. Sato, Equatorial inertia-gravity waves in the lower stratosphere  
513 revealed by TOGA-COARSE IOP data, *J. Met. Soc. Japan*, *77*, 721–736, 1999.

514 Xie, S., T. Hume, C. Jakob, S. A. Klein, R. B. McCoy, and M. Zhang, Observed large-  
515 scale structures and diabatic heating and drying profiles during TWP-ICE, *J. Climate*,  
516 *23*, 57–79, doi: 10.1175/2009JCLI3071.1, 2010.

517 Zhang, F., S. Wang, and R. Plougonven, Uncertainties in using the hodograph method  
518 to retrieve gravity wave characteristics from individual soundings, *Geophys. Res. Lett.*,  
519 *31*, L11,110, 2004.

520 Zhang, M. H., and J. L. Lin, Constrained variational analysis of sounding data based  
521 on column-integrated budgets of mass, heat, moisture, and momentum: approach and  
522 application to ARM measurements, *J. Atmos. Sci.*, *54*, 1503–1524, 1997.

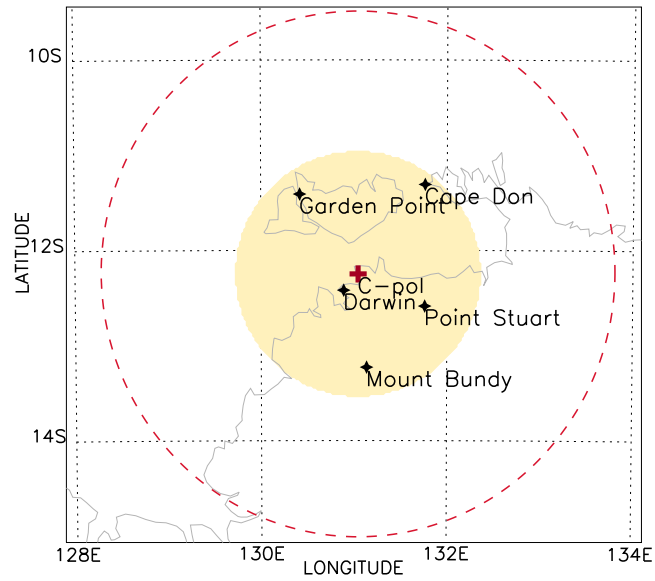


**Figure 1.** Observation sites during TWP-ICE. The shaded region centered at the cross sign marks the area covered by the C-pol radar data. The dashed circle shows the 300 km radius from the radar center.

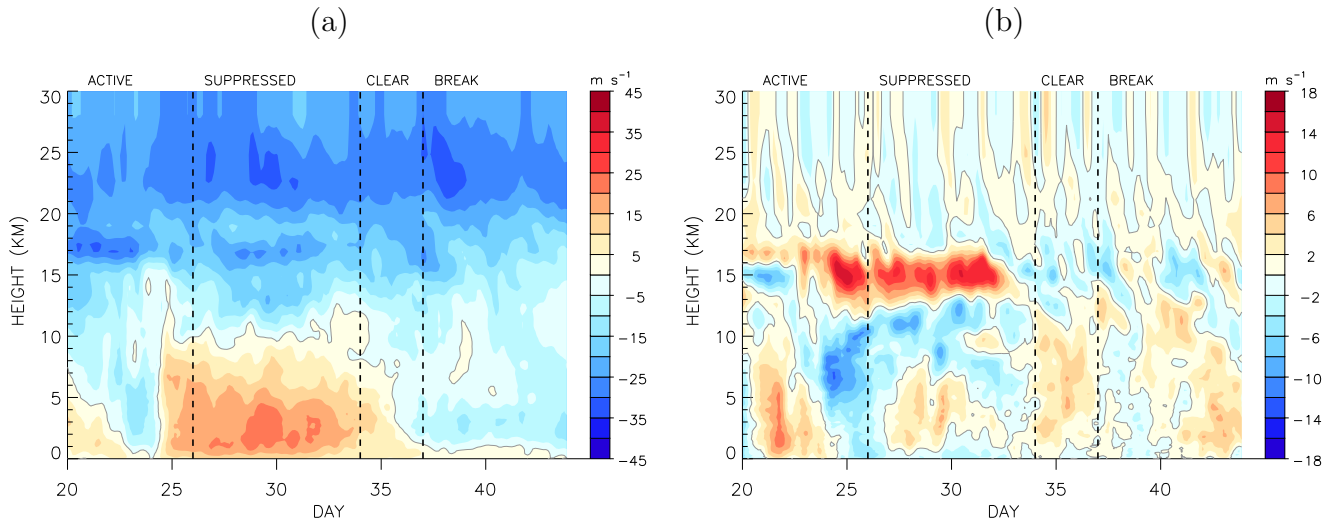


**Figure 2.** Time-height evolution of the mean (a) zonal and (b) meridional wind components provided by the variational analysis [Xie *et al.*, 2010]. The horizontal axis denotes day number in year 2006.

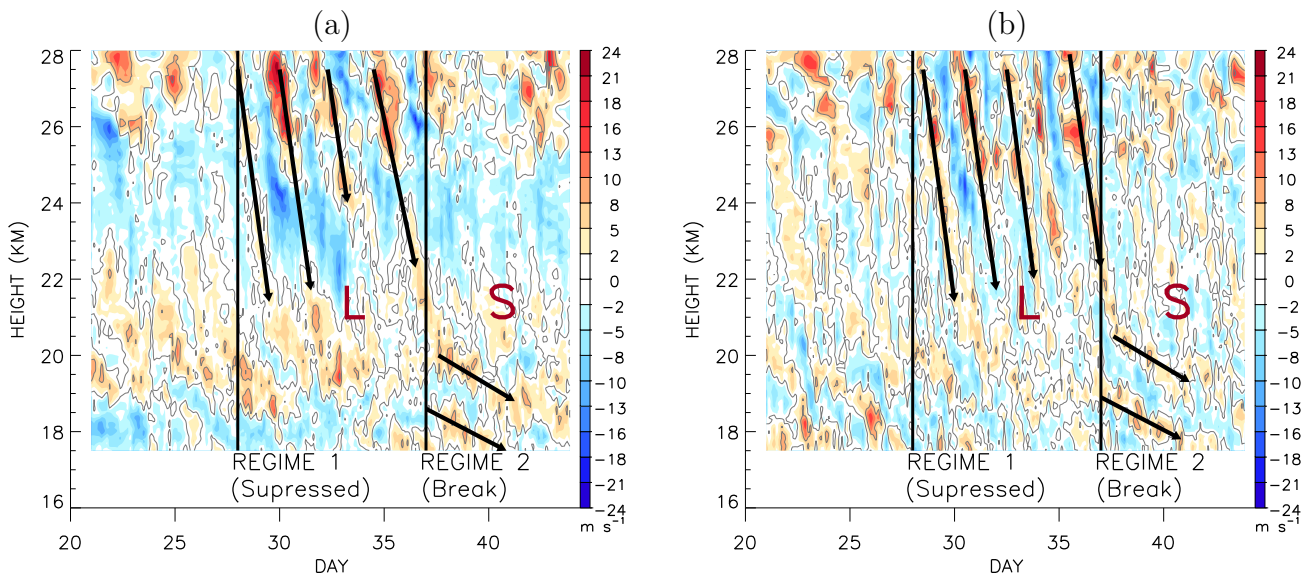


**Figure 3.** Time-height evolution of the zonal (a) and meridional (b) wind perturbations at the station Point Stuart. Positive values are contoured. The mean state is taken from the variational analysis. Arrows mark the descending phase propagation.

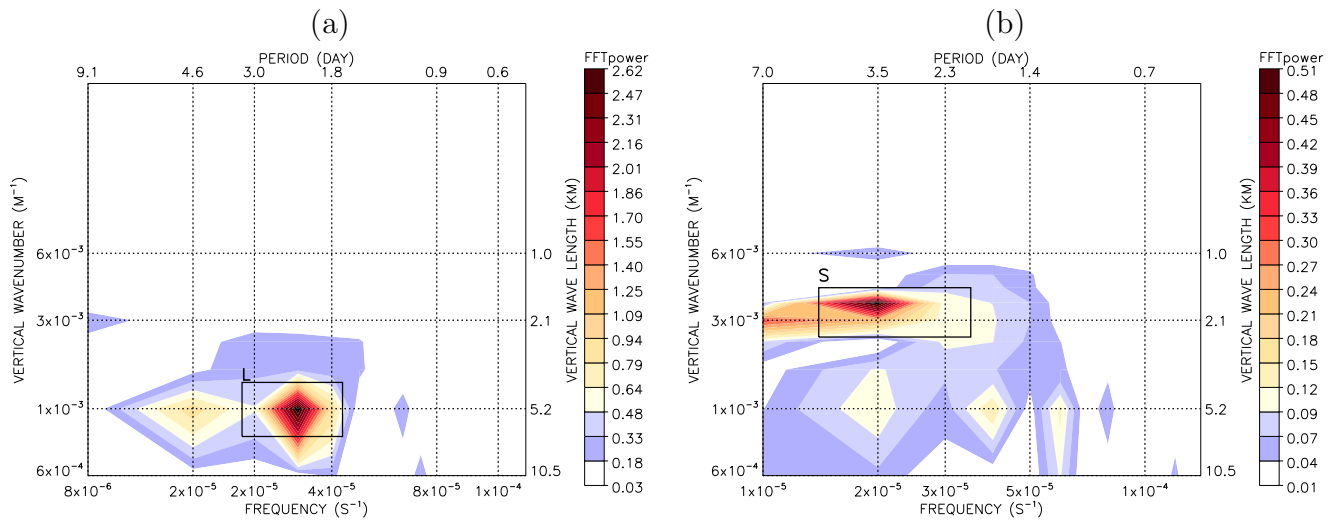


**Figure 4.** Two-dimensional quadrature spectra of the horizontal wind perturbations for Regime 1 (left) and Regime 2 (right).

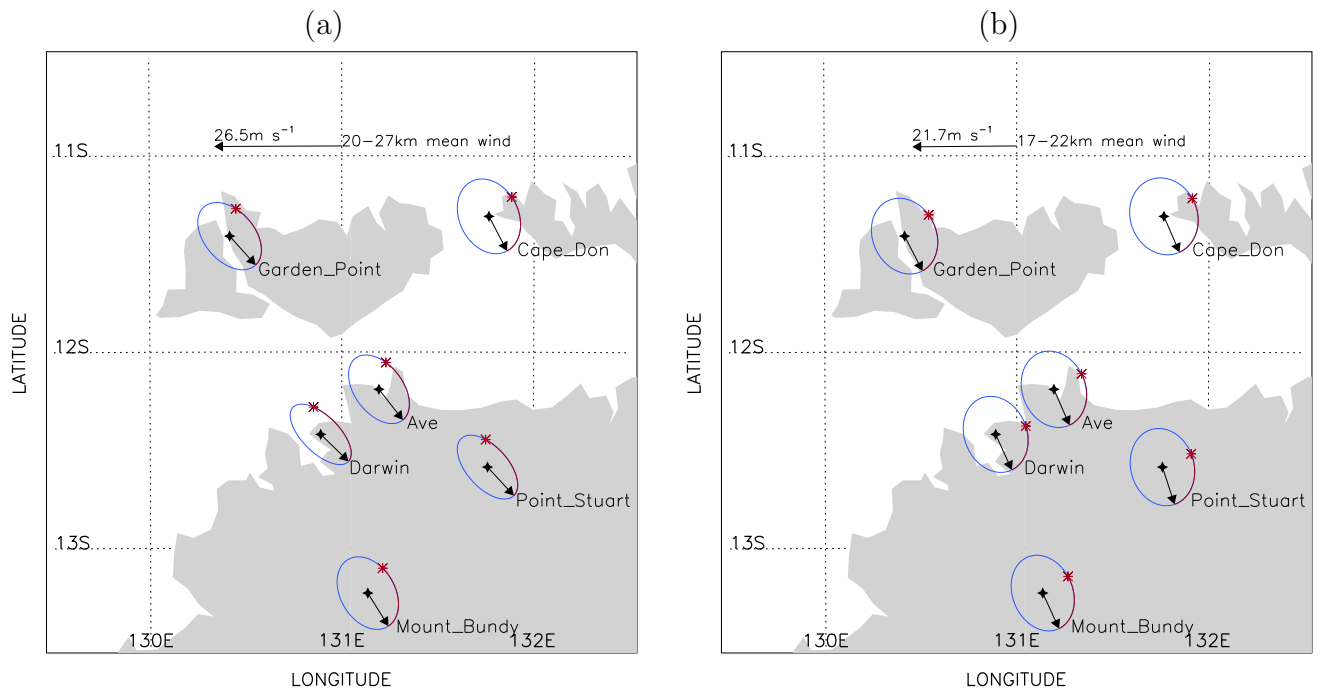


**Figure 5.** Polarization ellipses calculated using the Stokes parameter method for waves of group L (a) and S (b). Arrows point in the direction of the horizontal wave vectors. Phase differences  $\delta$  between  $v'$  and  $u'$  are shown by the arcs (red in the online version) starting from the heads of the vectors to the points marked by \* sign.

**Table 1.** Gravity wave properties calculated using Stokes parameters for waves WL and WS. ACW/CW is the ratio between anti-clockwise and clockwise rotating power spectra, signifying the ratio between upward and downward energy propagations.  $\bar{U}$  is the wind in the direction of the horizontal wave vector averaged over the duration and height range of each wave.  $\tau$  and  $\tau_*$  are the ground-based and intrinsic wave periods, respectively.  $\lambda_z$  is the vertical wavelength.  $\lambda_{disp}$  and  $\lambda_{dopp}$  are the horizontal wavelengths calculated from the dispersion relation (Eq. 6) and the doppler relation (Eq. 7), respectively.

Station	group L ( $\lambda_z \approx 5.2$ km, $\tau \approx 60$ h, $\bar{V}_z \approx -0.5$ m s <sup>-1</sup> km <sup>-1</sup> , 22-28 km)									
	d	$\delta$ (deg)	$\Theta$ (deg)	$\Theta_{(T'_{+90})}$ (deg)	$r$	ACW/ CW	$\bar{U}$ (m s <sup>-1</sup> )	$\tau_*$ (h)	$\lambda_{disp}$ (km)	$\lambda_{dopp}$ (km)
Cape Don	0.96	99.2	-18.2	-61.7	0.76	26.8	-12.6	43.3	4547	7025
Darwin	0.97	128.6	-50.1	-43.6	0.48	7.2	-19.2	26.6	2122	3310
Garden Point	0.98	114.3	-46.6	-47.6	0.65	17.2	-17.9	36.5	3308	5991
Mount Bundy	0.95	109.4	-45.7	-57.4	0.71	18.8	-14.3	40.0	3816	6171
Point Stuart	0.94	123.7	-40.6	-46.4	0.53	8.2	-18.3	29.8	2461	3906
Average	<b>0.96</b>	<b>115.0</b>	<b>-40.2</b>	<b>-51.3</b>	<b>0.63</b>	<b>15.6</b>	<b>-16.6</b>	<b>35.2</b>	<b>3263</b>	<b>5280</b>
Stdev	0.01	11.6	12.8	7.8	0.12	8.1	2.9	7.0	997	1590
Station	group S ( $\lambda_z \approx 1.8$ km, $\tau \approx 70.8$ h, $\bar{V}_z \approx 2$ m s <sup>-1</sup> km <sup>-1</sup> , 17.5-22 km)									
	d	$\delta$ (deg)	$\Theta$ (deg)	$\Theta_{(T'_{+90})}$ (deg)	$r$	ACW/ CW	$\bar{U}$ (m s <sup>-1</sup> )	$\tau_*$ (h)	$\lambda_{disp}$ (km)	$\lambda_{dopp}$ (km)
Cape Don	0.68	97.1	-59.2	-66.0	0.87	5.08	-9.0	48.1	2568	4828
Darwin	0.73	82.3	-109.5	-65.1	0.81	5.97	-9.3	44.3	1999	3949
Garden Point	0.67	101.2	-40.6	-62.4	0.82	4.83	-10.2	45.1	2090	4542
Mount Bundy	0.85	96.2	-77.1	-64.8	0.78	10.33	-9.4	42.6	1817	3622
Point Stuart	0.76	95.8	-74.6	-71.5	0.82	6.88	-7.0	45.1	2100	3129
Average	<b>0.74</b>	<b>94.5</b>	<b>-72.2</b>	<b>-66.0</b>	<b>0.82</b>	<b>6.62</b>	<b>-9.0</b>	<b>45.0</b>	<b>2115</b>	<b>4014</b>
Stdev	0.07	7.1	25.4	3.4	0.03	2.23	1.2	2.0	278	686

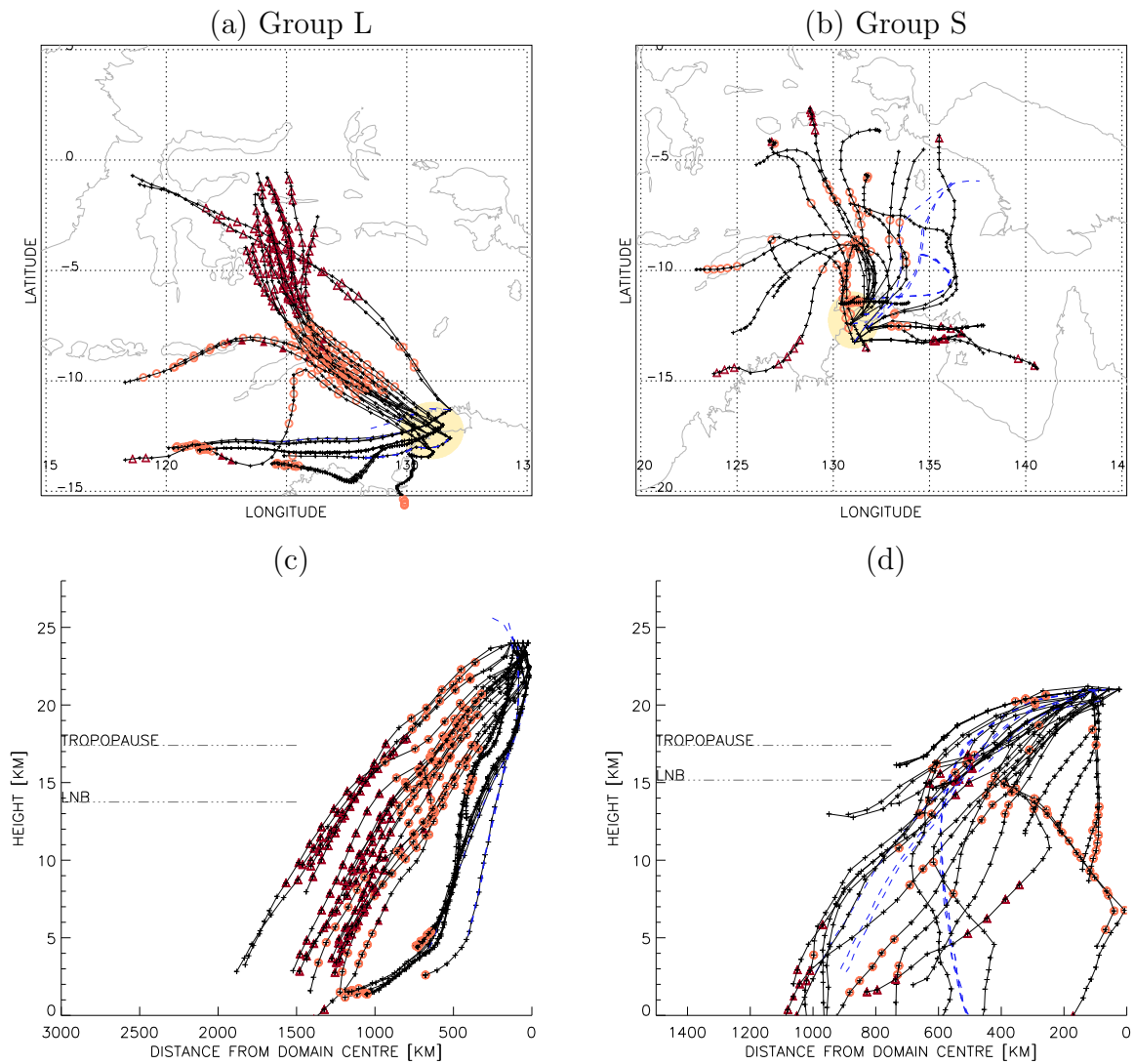


**Figure 6.** Backward ray-tracing for groups L (left panels, rays arriving at 00Z 04/02/2006) and S (right panels, rays arriving on 00Z 08/02/2006). (a,b) Horizontal plane view; (c,d) distance-height view. Black solid (dashed blue) lines show rays that do (do not) pass over regions with convective activity of deep (red triangles) and/or shallow (brown circles) convection. Shaded areas in a and b show the radar coverage during TWPICE. Distance is calculated from the location of C-Pol radar at (131.044 E,12.249 S).

**1 Gravity Waves Generated by Convection during**  
**2 TWP-ICE. Part II: High-Frequency Gravity Waves**

Mai C. N. Hankinson,<sup>1</sup> M. J. Reeder,<sup>1</sup> and T. P. Lane<sup>2</sup>

---

Mai C.N. Hankinson, School of Mathematical Sciences, Monash University, Wellington Road, Melbourne, Victoria 3800, AUSTRALIA. (Mai.C.Nguyen@monash.edu)

M. J. Reeder, School of Mathematical Sciences and ARC Centre for Excellence for Climate System Science, Monash University, Wellington Road, Melbourne, Victoria 3800, AUSTRALIA. (Michael.Reeder@monash.edu)

T. P. Lane, School of Earth Sciences and ARC Centre of Excellence for Climate System Science, The University of Melbourne, Victoria 3010, AUSTRALIA. (tplane@unimelb.edu.au)

<sup>1</sup>School of Mathematical Sciences,  
Monash University, Melbourne, Victoria,  
AUSTRALIA.

<sup>2</sup>School of Earth Sciences, The University  
of Melbourne, Victoria, AUSTRALIA.

3 **Abstract.**

4 High-frequency gravity waves are analyzed using radiosonde soundings taken  
5 during the Tropical Warm Pool - International Cloud Experiment (TWP-  
6 ICE) campaign. The intrinsic periods of these waves are estimated to be be-  
7 tween 20-40 minutes. The high-frequency wave activity in the stratosphere,  
8 defined by mass-weighted variance of the vertical motion of the sonde, has  
9 a maximum following the afternoon local convection indicating that these  
10 waves are generated by local convection. The wave activity is strongest in  
11 the lower stratosphere below 22 km and, during the suppressed monsoon pe-  
12 riod, is modulated with a 3-4-day period. The concentration of the wave ac-  
13 tivity in the lower stratosphere is consistent with the properties of the en-  
14 vironment in which these waves propagate, whereas its 3-4-day modulation  
15 is explained by the variation of the convection activity in the TWP-ICE do-  
16 main. At low rainfall intensity ( $<1 \text{ mm hr}^{-1}$ ), the wave activity increases as  
17 rainfall intensity increases. At high values of rainfall intensity, however, the  
18 wave activity associated with deep convective clouds is independent of the  
19 rainfall intensity.

20

## 1. Introduction

21 In Part I, the properties of inertia-gravity waves were analyzed from radiosonde obser-  
22 vations taken during the TWPIICE campaign. The present paper, Part II, focuses on the  
23 observations of the high-frequency gravity waves, which have intrinsic frequencies closer  
24 to the buoyancy frequency  $N$  and much greater than the inertial frequency  $f$ .

25  
26 In general, high-frequency gravity waves are difficult to observe as they tend to propa-  
27 gate rapidly upwards. Consequently, these waves are most commonly observed near the  
28 place and time of their generation. High-frequency gravity waves have been observed with  
29 radars [e.g. *Dhaka et al.*, 2005; *Uma et al.*, 2011; *Kaur et al.*, 2012] and satellites [e.g.  
30 *Sentman et al.*, 2003; *Hecht et al.*, 2009]. From radar data, the horizontal wavelength  
31 and frequency of the waves can be observed directly. However, these data are limited by  
32 the area covered by the radar. From satellite data (e.g. airglow images), the horizontal  
33 wavelength and ground-based phase velocity are observed directly. Although satellites  
34 cover large areas, the observations of the high-frequency gravity waves are contingent on  
35 the waves reaching the upper atmosphere (e.g at 80 - 100 km altitudes).

36  
37 Using radiosonde data, *Lane et al.* [2003]; *Geller and Gong* [2010]; *Gong and Geller*  
38 [2010] deduced the wave activity and frequencies of the high-frequency gravity waves.  
39 Radiosonde data are available globally and for long times, but they are limited by rel-  
40 atively coarse time resolution (typically 3 to 12 hours between two consecutive obser-  
41 vations). Moreover, the vertical wavelengths cannot be calculated from the sounding

42 directly [Reeder *et al.*, 1999; Lane *et al.*, 2003]. For all these reasons, there is a need for  
43 detailed observation of high-frequency gravity waves. Such observations are required to  
44 validate model studies and parameterization schemes [e.g. Chun and Baik, 1998; Beres  
45 *et al.*, 2002]. The main aspects of the high-frequency gravity waves addressed here include  
46 their vertical and temporal variations, and their relationship with the rain rate, which is  
47 a proxy for the diabatic heating rate.

48  
49 The remainder of the paper is organized as follows. The observations and data analysis  
50 are described in Section 2. The properties of the high-frequency gravity waves (including  
51 their periods, vertical and horizontal wavelengths) are analyzed in Section 3. The temporal  
52 and vertical variations in the wave activity and its relationship with the rain rate are  
53 presented in Section 4. Section 5 explains the observed variations of the wave activity  
54 by examining the properties of the environment for wave propagation and the variation  
55 of the convective sources in the vicinity of TWPICE. Finally, conclusions are given in  
56 Section 6.

## 2. Data

57 The radiosonde data taken during TWPICE have been described in Part I and, hence,  
58 are not repeated here. Figure 1, showing the locations of the observation stations dur-  
59 ing TWP-ICE, is reprinted here for convenience. As in Part I, two weather regimes are  
60 analyzed separately. Regime 1 is the period from 28 January to 6 February 2006 char-  
61 acterized by a suppressed monsoon, while Regime 2 is the monsoon break from 7 to 13  
62 February 2006. The remainder of this section describes the calculation of the vertical

63 velocity perturbations, from which the properties of the high-frequency gravity waves are  
64 deduced, and the radar and satellite data used to define the convective activity.

## 2.1. Perturbations of vertical velocity derived from radiosonde soundings

65 Properties of the high-frequency gravity waves are derived from perturbations in the  
66 ascent rate of the balloon using the method described by *Lane et al.* [2003], *Gong and*  
67 *Geller* [2010], and *Geller and Gong* [2010]. The ascent rate of the balloon is calculated  
68 from the time derivative of the altitude of the balloon, which is itself determined using  
69 the hypsometric equation. The wave perturbations of vertical velocity  $w'$  are defined as  
70 the deviations from the background ascent rate. The assumption underpinning the anal-  
71 ysis is that these perturbations in the ascent rate are a result of high-frequency gravity  
72 waves. The perturbations are obtained by first fitting and then subtracting a polynomial  
73 from each vertical profile of the ascent rate. Since perturbations in the troposphere con-  
74 tain signals from processes other than gravity waves such as turbulence and convection,  
75 the analysis of the gravity waves is carried out in the stratosphere from 17.5 to 28 km  
76 (the tropopause is located near 17 km during the campaign). The perturbations in the  
77 stratosphere are calculated as departures from a cubic polynomial, though the order of  
78 the polynomial does not affect the results qualitatively (as will be discussed in Section  
79 4.1). In addition, perturbations of vertical velocity in the troposphere (examined between  
80 3 and 10 km) are used in Section 4.2 to relate the wave activity of high-frequency gravity  
81 waves in the stratosphere with its possible source of tropospheric convective activity. For  
82 the troposphere, the perturbations are calculated by removing a linear least-square fit  
83 to the vertical profile. The linear fit is chosen here rather than a high-order polynomial

84 because of the ambiguities introduced by convective clouds.

85

## 2.2. Precipitation estimates from radar

86 Precipitation estimates from C-pol radar (the description of which can be found in  
87 *Keenan et al.* [1998]) are available every 10 minutes on a  $2.5 \times 2.5$  km grid. The area cov-  
88 ered by these data is shown as the shaded region in Figure 1. In addition to the rainfall  
89 rates, rainfall type (either convective, stratiform or mixed), as determined by the method  
90 developed by *Steiner et al.* [2004], is available at each grid point. The rainfall amount  
91 and area for each type are accumulated over the 3-hour periods prior to the observation  
92 times. These data will be used in Section 4 to relate the activity of high-frequency waves  
93 to the diabatic heating implied by the rainfall estimated from the C-pol radar.

94

## 2.3. Convective activity estimated from satellite

95 Infra-red measurements from the MTSAT satellite are used to quantify the convective  
96 activity in the areas surrounding the TWPICE domain to complement the radar obser-  
97 vations. Convection is identified by the method of *Inoue* [1987]. Deep convection is  
98 assumed where the brightness temperature of the IR1 channel ( $10.3\text{-}11.3 \mu\text{m}$ ) is lower  
99 than a threshold value  $\text{IR1}_{top}$ , which signifies that the cloud top is above the middle tro-  
100 posphere, and the difference between channels IR1 and IR2 ( $11.5\text{-}12.5 \mu\text{m}$ ) is less than  
101  $0.5^\circ\text{C}$ .  $\text{IR1}_{top}$  is chosen to be  $-10^\circ\text{C}$  which is above the 500 hPa level for TWPICE. Shal-  
102 low convection is identified when the brightness temperature on channel IR1 lies between  
103  $\text{IR1}_{top}$  and  $2^\circ\text{C}$ , and the (IR1-IR2) difference in the brightness temperatures is less than

104 1°C. These estimates of the convective activity are used to infer the tropospheric source  
 105 of the gravity waves (Section 5).

### 3. Properties of High-Frequency Gravity Waves

#### 3.1. Frequency

107 Following *Geller and Gong* [2010], the intrinsic frequency, and hence the intrinsic period,  
 108 is calculated from the ratio of perturbation vertical kinetic energy  $V = \frac{1}{2}\overline{w'^2}$  to the  
 109 perturbation potential energy  $P = \frac{1}{2}\overline{(g^2/N^2)(T'/T_0)^2}$ . In the expressions for  $V$  and  $P$ ,  
 110  $g$  is the gravitational acceleration,  $T_0$  is the temperature of the mean state, which is  
 111 taken from the variational analysis [*Xie et al.*, 2010] as described in Part I, temperature  
 112 perturbation  $T'$  is the deviation from the mean state, and the overbar denotes averaging  
 113 in the vertical over all stations at a particular time. The relationship between  $V/P$  and  
 114 the intrinsic frequency is (using Eq. B6 of *Geller and Gong* [2010])

$$b \left( \frac{N^2}{\omega_*^2} \right)^2 - \left( \frac{b}{V/P} + 1 \right) \frac{N^2}{\omega_*^2} + 1 = 0 \quad (1)$$

115  
 116 where  $b = m^2 H_s^2 + 1/4$ ,  $m$  is the vertical wavenumber,  $\omega_*$  is the intrinsic frequency, and  $H_s$   
 117 is the density scale height. The intrinsic frequencies calculated from all soundings using  
 118 Eq. 1 have a mean of 33 minutes and a standard deviation of 8 minutes. Note that the  
 119 hydrostatic version ( $\omega_*^2 = N^2 V/P$ ) gives very similar values to those from Eq. 1.

120  
 121 The intrinsic frequencies have also been calculated using the 1.7-day high-pass filtered  
 122 temperature perturbations to eliminate the contributions from the low-frequency waves

123 (see Part I). The resultant frequencies have a mean of 24 minutes and a standard deviations  
124 of 6 minutes, which are relatively close to the estimates using the unfiltered perturbations.  
125 Thus, based on this analysis the mean intrinsic periods of the high-frequency gravity waves  
126 lay in the range 20 to 40 minutes.

127

### 3.2. Vertical and horizontal wavelengths

128 One way to directly calculate the vertical wavelengths  $\lambda_z$  of the high-frequency gravity  
129 waves in the stratosphere is from a Fourier transform of the  $w'$  vertical profiles. This  
130 approach gives a the mean  $\lambda_z$  of around 1.2-2 km. In addition, during the campaign, the  
131 spectrum of  $\lambda_z$  fluctuates in a pulse-like manner, peaking and broadening (towards the  
132 longer wavelengths) near the times of maximum precipitation. With an intrinsic frequency  
133 of 20-40 minutes and a vertical wavelength of around 2 km, the dispersion relation could  
134 be used (e.g.  $\omega_*^2 = N^2 k_h^2 / (m^2 + k_h^2)$ , where  $k_h$  is the horizontal wavenumber to estimate  
135 the horizontal wavelength ( $\lambda_h = 2\pi/k_h$ ). Such a calculation would give a value of the  $\lambda_h$   
136 around 15-30 km.

137

138 However, as pointed out by *Gardener and Gardener* [1993], *Reeder et al.* [1999] and  
139 *Lane et al.* [2001], vertical wavelengths estimated from the ascent rate of the balloon are  
140 prone to large errors whenever the horizontal winds are strong, the period is short, or  
141 the horizontal wavelengths are short. According to these authors, two conditions must be  
142 satisfied before the radiosonde sounding can be used to accurately calculate the vertical  
143 wavelength from spectral analysis. These conditions are

$$\left| \frac{\lambda_z \bar{U}}{\lambda_h \bar{W}} \right| \ll 1 \quad \text{and} \quad \frac{\lambda_z}{\tau \bar{W}} \ll 1 \quad (2a,b)$$

144 where  $\bar{W}$  is mean ascent rate and  $\tau = 2\pi/\omega$  is the ground-based period. In cases of  
 145 strong horizontal winds and/or short horizontal wavelengths,  $\lambda_z$  may be greatly underes-  
 146 timated. For the waves investigated here:  $\lambda_z \approx 2$  km,  $\lambda_h \approx 15$  km,  $U \approx 20$  m s<sup>-1</sup>,  $\bar{W} \approx 5$   
 147 m s<sup>-1</sup>, and  $\tau \approx 30$  minutes, resulting in the ratios of 0.53 and 0.2 for the inequalities 2a  
 148 and 2b, respectively. Therefore, the inequalities 2 are not well satisfied, and consequently  
 149  $\lambda_z$  and  $\lambda_h$  cannot be determined directly from the radiosonde profiles.

#### 4. Properties of the wave activity

151 To investigate the connection between convection and the high-frequency gravity waves,  
 152 the wave activity as measured by the density-weighted variance of the perturbations of  
 153 vertical velocity  $\rho w'^2$  is examined.

##### 4.1. Vertical and temporal variation of the wave activity

155 Figure 2a shows the time-height evolution of the wave activity (derived from the ascent  
 156 rate) averaged over all stations during Regimes 1 and 2. The strongest wave activity is  
 157 concentrated in the layer below 22 km, indicating that the layer above filters the waves.  
 158 Furthermore, the time series of the wave activity averaged over heights of 17.5-28 km ex-  
 159 hibits a pulse-like pattern. This temporal variation of the 17.5-28 km mean wave activity  
 160  $\overline{\rho w'^2}$  is analyzed using a Morlet wavelet transform, the results of which are plotted in Fig-  
 161 ure 2b. During Regime 1, the wave activity varies predominantly with a 3-4 day period,

162 but varies mostly with a 1-day period during Regime 2. While the 1-day period variation  
 163 of the high-frequency gravity wave activity can be explained by the diurnal variation of  
 164 the convection during the monsoon break (Regime 2), the origin of the 3-4-day period  
 165 variation during Regime 1 is less clear and will be investigated in Section 5.

166

167 The sensitivity of the wave activity to the background profile used for the calculation of  
 168 the vertical velocity perturbations is examined now. Figure 3 shows the variation of the  
 169 wave activity computed using the vertical velocity perturbations obtained by removing  
 170 different background profiles. In the lower stratosphere from 17.5 to 22 km (panel a),  
 171 values of the wave activity calculated using linear, quadratic and quartic polynomials to  
 172 define the background state are 18%, 6% larger and 2% smaller, respectively, than that  
 173 using a cubic polynomial. In addition, an application of a box-car smoothing after re-  
 174 moving a fitted cubic polynomial increases the wave activity by 7%. In the upper part of  
 175 the stratosphere from 22 to 28 km (panel b), the wave activity calculated with different  
 176 background profiles differs by less than 6% from that based on a cubic polynomial. Im-  
 177 portantly, the patterns of wave activity calculated with different background profiles are  
 178 similar to each other (see both panels in Figure 3). Thus, the order of the polynomial  
 179 chosen to define the background state does not qualitatively affect the results.

180

## 4.2. Diurnal variation of the wave activity

181 A diurnal composite of the area-averaged precipitation rates estimated by the C-pol  
 182 radar during Regime 2 is shown in Figure 4. The time series of the precipitation rate  
 183 has two maxima; the smaller peak is in the afternoon at 1830 local time (LT = UTC

184 + 0930 hrs) and the larger peak is in the early morning at 0630 LT. Regime 1 has a  
185 similar pattern (not shown) but a much weaker diurnal variation. Moreover, the spatial  
186 distribution of the precipitation types (not shown) reveals a clear difference between the  
187 afternoon and early morning; during the afternoon, the precipitation is convective and  
188 located over land, whereas in the morning it is predominantly stratiform and located over  
189 the sea. This distribution for Darwin area is found also by *Vallgren* [2006], who used the  
190 number of convective cells detected by radar reflectivity as the measure of convective ac-  
191 tivity. Although the early morning precipitation covers a large area, it is mainly stratiform.

192  
193 The diurnal variation of  $\overline{\rho w'^2}$  in the troposphere (3-10 km) and lower stratosphere  
194 (17.5-22 km) are plotted also in Figure 4. While  $\overline{\rho w'^2}$  in the lower stratosphere largely  
195 represents the wave activity, its counterpart in the troposphere may include the effects of  
196 other processes such as turbulence and convection. In the troposphere, the maximum of  
197  $\overline{\rho w'^2}$  occurs at 1530 LT, which is just prior to the afternoon precipitation maximum. In  
198 contrast, the early morning maximum in the precipitation at 0630 LT corresponds only to  
199 a weak increase in the tropospheric  $\overline{\rho w'^2}$ . The wave activity in the stratosphere shows one  
200 peak at 1830-2130 LT, which lags the afternoon precipitation maximum by 3 hours. This  
201 lag in the stratospheric wave activity suggests that the gravity waves in the stratosphere  
202 are generated by convection in the troposphere. Nevertheless, the 3-hour lag should not  
203 be viewed simply as the time taken for the gravity waves to propagate from troposphere  
204 to the stratosphere as the time resolution of the data is 3 hours. Large values of  $\overline{\rho w'^2}$   
205 in the troposphere are most likely attributable to turbulence and convection, which may

206 occur well before the generation of gravity waves.

207  
208 The reason for the absence of a stratospheric maximum in the wave activity following the  
209 early morning precipitation maximum is examined now. Assuming that high-frequency  
210 gravity waves are generated by convection, this difference between the precipitation and  
211 wave activity may be because the early morning maritime clouds are more stratiform and  
212 are presumably weaker generators of gravity waves, and/or the early morning environ-  
213 ment filters upward propagating waves. The first possibility is consistent with the C-pol  
214 radar data which shows that stratiform rainfall peaks at the early morning hours and  
215 covers an area roughly twice as large as the area covered by convective rainfall (not plot-  
216 ted). The prevalence of stratiform rainfall during early morning is supported also by the  
217 work of *Wapler and Lane* [2012]. Using WRF high-resolution simulations of the monsoon  
218 break period during TWP-ICE, *Wapler and Lane* [2012] showed that the early morning  
219 maritime clouds were initiated by the land breeze. These clouds are relatively shallow,  
220 and hence, unlikely to generate large-amplitude gravity waves. The second possibility has  
221 been examined also by comparing the differences in mean flows in the early morning and  
222 early afternoon. The differences in the mean zonal wind profiles are small, less than 5 m  
223  $s^{-1}$  (not shown), and are unlikely to be the cause of the observed differences in the wave  
224 activity in the stratosphere.

### 4.3. Relationship of the wave activity with the rainfall intensity

226 Variations in the diabatic heating in convective clouds is thought to be one of the  
227 mechanisms by which convection generates gravity waves [e.g. *Salby and Garcia*, 1987;

228 *Bretherton, 1988*]. For this reason, the relationship between the stratospheric wave ac-  
229 tivity and the convective rainfall intensity, which is a proxy for the diabatic heating by  
230 convection, is examined now.

231

232 Figure 5 shows scatter plots of the stratospheric wave activity averaged over the layers  
233 17.5-22 km and 22-28 km as a function of cube root of the convective rainfall intensity.  
234 (Here the cube root of the rainfall is used because it makes the distribution closer to  
235 normal.) The convective rainfall intensity is the average of the convective rain rates over  
236 convective rainfall areas detected by the C-pol radar. The data are stratified according  
237 to the cloud type identified by the variational analysis. Deep clouds are defined as those  
238 with tops above 5 km and depths more than 1 km. All other clouds are defined to be  
239 shallow.

240

241 Figure 5 shows that the relationship between the wave activity and convective rainfall  
242 intensity is not a simple linear relationship. At low rainfall intensity (e.g. less than 1  
243 mm h<sup>-1</sup>), the wave activity increases as the rainfall intensity increase in both the lower  
244 (panel a) and upper (panel b) layers. This relationship changes markedly at high rainfall  
245 intensity as the wave activity becomes largely independent from the rainfall intensity.  
246 Furthermore, although the rainfall intensity is lower during Regime 1, the independence  
247 of the wave activity from the rainfall intensity holds during both regimes (for cube roots  
248 of the rainfall intensity in the range of 1-1.5 mm h<sup>-1</sup> during Regime 1 and 1.5-2 mm h<sup>-1</sup>  
249 during Regime 2). Note also that the high rainfall intensity during Regime 2 is associated

250 with deep convection (marked by filled red triangles).

251

252 Differences in the wave activity in the lower and upper layers can be seen by comparing  
 253 panels a and b of Figure 5. During Regime 1 (open symbols), the wave activity in the  
 254 lower layer (panel a) of both shallow and deep convection types is much larger than that  
 255 in the upper layer (panel b). This decrease in the wave activity from the lower to the  
 256 upper layer implies that some filtering may have taken place in the upper layer. In con-  
 257 trast, during Regime 2 (filled symbols), values of the wave activity associated with deep  
 258 convection (red triangles) in the lower and upper layers are of similar magnitudes, indi-  
 259 cating that the waves propagate from the lower to the upper layer without being filtered  
 260 significantly.

261

## 5. Modulation of the High-Frequency Wave Activity

262 In this section the role of the background wind and potential temperature profiles in  
 263 the lower stratosphere in filtering vertical propagating waves is explored. The reason for  
 264 the 3-4-day period variation of the wave activity during Regime 1 is investigated also.

265

### 5.1. Variation in the propagation properties of the medium

266 The properties of the medium through which small-amplitude gravity waves propagate  
 267 is characterized by the Scorer parameter  $L^2$ , which is defined by

$$L^2 = \frac{N^2}{(c - U)^2} + \frac{U_{zz}}{(c - U)} - \frac{1}{H_s} \frac{U_z}{(c - U)} - \frac{1}{4H_s^2} \quad (3)$$

268

269 where  $c$  is the ground-based phase speed of the wave,  $U$  is the component of the environ-  
 270 mental wind in the direction of propagation, and the subscript  $z$  denotes the derivative in  
 271 the vertical direction. The first, second and third terms in  $L^2$  are commonly referred to  
 272 as the buoyancy term, the curvature term and the shear term, respectively. The Taylor-  
 273 Goldstein equation, which describes two-dimensional, linear disturbances in a horizontally  
 274 homogeneous, non-rotating, stably stratified atmosphere, can be written as

$$\frac{d^2\hat{w}}{dz^2} + (L^2 - k_h^2)\hat{w} = 0 \quad (4)$$

275

276 where  $k_h$  is the magnitude of horizontal wavenumber,  $\hat{w} = e^{-z/2H_s}\tilde{w}$  is the density-  
 277 weighted amplitude of the vertical velocity, and  $\tilde{w}$  is the amplitude of the vertical compo-  
 278 nent of the velocity [Nappo, 2002]. The Taylor-Goldstein equation requires  $(L^2 - k_h^2)$  to  
 279 be positive for wave-like solutions. Consequently, the square root of the Scorer parameter  
 280 is the largest horizontal wavenumber permitted to propagate vertically unimpeded in the  
 281 given environment. In other words, only waves with horizontal wavelengths larger than  
 282 the critical horizontal wavelength  $\lambda^* = 2\pi/|L|$  will propagate vertically.

283

284 The methods described in Section 3.1 permit the calculation of the intrinsic frequency  
 285 and the wave activity for the high frequency part of the spectrum. However, as inequali-  
 286 ties 2 are not satisfied, the horizontal and vertical wavenumbers cannot be calculated from  
 287 the radiosonde profiles. Consequently, the vertical and horizontal phase speeds are not  
 288 known. For this reason, the critical wavelength is calculated for all ground-based phase

289 speeds between  $-40$  and  $+40 \text{ m s}^{-1}$  and in all directions. The results of these calculations  
 290 for Regimes 1 and 2 in the layers 18-20 km and 24-26 km are shown in Figure 6. The wind  
 291 and potential temperature profiles used to construct Figure 6 come from the variational  
 292 analysis and are averaged for days 31-33 to represent Regime 1 and days 38-40 to rep-  
 293 resent Regime 2. Waves propagating upward and downstream may reach critical levels,  
 294 i.e., the level at which  $c = U$ . As a wave propagates upwards and approaches a critical  
 295 level, the ground-based frequency is conserved (provided the environment is stationary).  
 296 The intrinsic frequency is doppler-shifted by the background wind to zero and the wave is  
 297 either absorbed, reflected or partially transmitted depending on the details of the environ-  
 298 ment. Waves propagating upstream (to the east) require larger horizontal wavelengths to  
 299 propagate vertically than those propagating downstream (in the absence of critical levels).

300

301 The critical horizontal wavelength for the upper layer during Regime 1, denoted  $\lambda_{R1U}^*$ ,  
 302 is plotted as a function of ground-based phase speed in Figure 6a. In general,  $\lambda^*$  increases  
 303 as the phase speed in the zonal direction increases. Consequently, the horizontal wave-  
 304 length of upward propagation waves travelling to the west can be shorter than upward  
 305 propagating waves traveling to the east. For example,  $\lambda^* = 12 \text{ km}$  when the phase speed  
 306 is  $20 \text{ m s}^{-1}$  to the east whereas  $\lambda^* = 1 \text{ km}$  when it is  $20 \text{ m s}^{-1}$  to the west.

307

308 Figures 6b, c and d show how  $\lambda^*$  changes with layer and regime. The difference between  
 309  $\lambda_{R1U}^*$  (Figure 6a) and that in Regime 2, denoted  $\lambda_{R2U}^*$ , is plotted in Figure 6b. Likewise,  
 310 the difference between  $\lambda_{R1U}^*$  and  $\lambda^*$  in the lower layer during Regime 1,  $\lambda_{R1L}^*$ , is plotted in  
 311 Figure 6c, while the difference between  $\lambda_{R1U}^*$  and  $\lambda^*$  in the lower layer in Regime 2,  $\lambda_{R2L}^*$ ,

312 is plotted in Figure 6d.  $\lambda^*$  in the upper layer changes little from Regime 1 to Regime 2.  
313 In contrast, in the lower layer,  $\lambda^*$  is much smaller during Regime 2 compared to Regime 1.  
314 In other words, during Regime 2, the lower stratosphere is more favorable for the vertical  
315 wave propagation of high-frequency gravity waves than during Regime 1. In addition,  
316 negative differences (i.e. smaller  $\lambda^*$  in the lower layer than in the upper layer) in panels  
317 c and d indicate that the upstream waves with shorter wavelengths are attenuated while  
318 propagating upwards (through the upper layer). This attenuation is consistent with the  
319 decrease in the high-frequency wave activity in the upper stratosphere shown in Figs. 2a  
320 and 5.

321  
322 To illustrate the effects of the environmental wind and temperature in the lower strato-  
323 sphere in attenuating the high-frequency wave activity, Figure 7 shows the time-height  
324 evolution of the critical horizontal wavelength for waves with phase speed of  $20 \text{ m s}^{-1}$   
325 towards the east. This value is chosen close to the phase speed corresponding to a crit-  
326 ical wavelength of 15 km (see Figure 6a), which is typical for horizontal wavelengths of  
327 the convectively-generated gravity waves simulated by numerical models [see e.g. *Lane*  
328 *et al.*, 2001]. Such a wave propagates against the mean wind in the 18-20 km layer and,  
329 according to Figure 6, in an environment in which the critical wavelength increases with  
330 height. Moreover, all things being equal, waves propagating upstream will have larger  
331 amplitudes (in vertical velocity) than those propagating downstream [*Lane et al.*, 2001;  
332 *Beres et al.*, 2002], and hence, the effect of the environment on wave activity should be  
333 most pronounced for these waves. The important point of Figure 7 is that the high-  
334 frequency wave activity between 17.5 and 22 km is much larger than that between 22 and

335 28 km, and that this decrease is accompanied by an increase in the critical wavelength.  
336 This general pattern is not dependent on the choice of phase speed, and is consistent with  
337 the observed distribution of the high-frequency wave activity, which is concentrated in  
338 the lower stratosphere below about 22 km (see Figure 2a). The largest contribution to  
339 the Scorer parameter comes from the buoyancy term, which is of order  $10^{-6} \text{ m}^{-2}$ . At a  
340 height of 20 km, the curvature and shear terms are of order  $10^{-7} - 10^{-6}$  and  $10^{-8} \text{ m}^{-2}$ ,  
341 respectively, while at 24 km, the curvature and shear terms are of order  $10^{-12}$  and  $10^{-9}$   
342  $\text{m}^{-2}$ , respectively. At times, the curvature term at 20 km makes a significant contribu-  
343 tion, reaching the same order of magnitude as the buoyancy term, increasing the Scorer  
344 parameter and reducing the critical wavelength.

345

## 5.2. Variation in the wave source

346 Although the 3-4-day variation of the wave activity during Regime 1 appears in Figure  
347 7 as three peaks in the wave activity on days 28-29, 31-33 and 35-36 (which correspond to  
348 28-29 January, 31 January - 2 February and 4-5 February 2006), the critical wavelength in  
349 the lower stratosphere does not show a similar variation in time. For instance, the peak on  
350 day 36 is not associated with a smaller value of  $\lambda^*$ . It appears, therefore, that the 3-4-day  
351 variation in the wave activity cannot be explained by the variation of the environment  
352 through which these waves propagate and is likely related to variations in the wave source.

353

354 The variation in the source of the waves and its connection to the 3-4-day variation is  
355 examined now. Figure 7 shows the evolution of convection as represented by the area-  
356 averaged convective rain rates estimated from the C-pol radar reflectivity and the coverage

of deep convection using IR satellite imagery from MTSAT. The plotted rain rates are averaged over the radar scan area, which is within 150 km radius from Darwin. The 3-4-day variation in the wave activity appears related to the variation in the area covered by deep convection within about 150-300 km of Darwin with peaks during days 31-33 and 35-36. Within a radius of 150 km, the radar-derived rain rates and the area covered by deep convection show only the first peak. Hence, it seems likely that the second peak in the wave activity is generated by the convection outside of the area covered by the radar.

To test the possibility that some of the high-frequency gravity waves detected in the TWP-ICE radiosondes are generated outside of the area covered by the radar, rays are traced backwards in time using the code GROGRAT [Marks and Eckermann, 1995]. The wind and temperature fields used to define the environment come from the 6-hourly ERA Interim reanalysis. Ray tracing is done for waves with horizontal wavelengths of 7, 15, 25 km, from all directions in steps of 45 degrees (i.e. 0, 45, 90, 135, 180, 225, 270 and 315 degrees), and intrinsic periods of 15, 25 and 40 minutes, which are similar to the estimates in Section 3.1. Rays are released backward in time at 22 km altitude, from four locations in the TWPIECE domain (130E, 13S), (131.1E, 13.23S), (131E, 12.5S), and (131.8E, 11.3S). Rays arriving the TWP-ICE domain at 00Z on day 36, plotted in Figure 9a, come mostly from west and south-west quadrant. Figure 9b shows the rays in terms of height and the distance from the C-pol radar. Among these rays, several originate in the middle troposphere outside of the C-Pol radar area. Moreover, using the IR satellite data, convection is found along the rays coming from the south-west (panel a) in the mid-to-upper part of the troposphere (panel b). (In a study based on observations taken in Korea, the

380 6-13 km layer in the middle troposphere was also identified by *Ki and Chun* [2011] as the  
381 height range from which the convectively-generated gravity waves originated.) Thus, the  
382 backward traced rays presented here support the possibility that the small peak in the  
383 wave activity on days 35-36 is related to the convection from outside of the TWP-ICE  
384 domain. In addition, most of rays traced backwards from the first peak during days 31-  
385 33 (not shown) come from the area with deep convection within the TWP-ICE domain.  
386 These ray-tracing results are consistent with the concurrence of the peaks in the wave  
387 activity and the rain rates, and hence, supporting idea that the main contribution to the  
388 peak in the wave activity during days 31-33 comes from the convection within the domain.

389  
390 As discussed by *Berry et al.* [2012], about half of the rainfall in the Australian sum-  
391 mer monsoon is related to the passage of low-level, cyclonic potential vorticity anomalies.  
392 Figure 9 shows the time-latitude Hovmöller diagram of the potential vorticity in the layer  
393 between the 310-320 K isentropic surfaces. This layer is located near 700 hPa level, at  
394 which cyclonic PV is typically produced by tropical convection. The first and second peaks  
395 in the wave activity correspond to the enhanced cyclonic potential vorticity (marked by  
396 letters A and B, respectively, in Figure 9). In particular, the second peak is associated  
397 with the region of enhanced cyclonic potential vorticity which extends to the south of  
398 Darwin. Thus, the periods of enhanced cyclonic potential vorticity are consistent with  
399 the convection coverage derived from satellite imagery. Moreover, it appears that the  
400 second peak was generated by the convection outside the area of TWP-ICE and that the  
401 3-4 day variation in the wave activity reflects the temporal variation in cyclonic potential

vorticity anomalies in the region and their associated convection.

## 6. Conclusions

The properties of high-frequency gravity waves were determined from the fluctuations in the ascent rate of the radiosondes released during the TWICE campaign. The intrinsic period of these waves was found to be in the range of 20-40 minutes using the method of *Geller and Gong* [2010].

The wave activity was quantified by the mass-weighted variance of the vertical motion ( $\overline{\rho w'^2}$ ). The wave activity was strongest in the lower part of the stratosphere below 22 km and varied with a distinct 3-4-day period during the suppressed monsoon regime, and with a one-day period during the monsoon break regime. Moreover, the diurnal variation of the wave activity in the stratosphere was larger following the afternoon local convection, indicating that these gravity waves were generated by local convection. At rainfall intensity less than about  $1 \text{ mm hr}^{-1}$  the wave activity increased roughly linearly with the cube root of the rainfall intensity, which is a proxy for diabatic heating by the convection. At higher rainfall intensity there appeared to be no clear relationship between the wave activity and diabatic heating. During Regimes 2, the highest rainfall intensity was generally associated with deep convective clouds and the wave activity was largely independent of height.

The 3-4-day modulation of the wave activity during the suppressed monsoon regime and its concentration in the lower part of the stratosphere was investigated by examining the

424 propagation properties of the medium and the time-variation of the wave source. It was  
425 found that the propagation properties (as measured by the Scorer parameter) of the layer  
426 between 22-26 km were not favorable for short waves propagating to the east (upstream).  
427 Thus, the presence of this layer was consistent with the decrease of the wave activity  
428 with height. The 3-4-day variation was found to be consistent with the variation of the  
429 convection activity in the region within 300 km of the TWP-ICE domain, which was also  
430 related to the variability in synoptic scale potential vorticity anomalies.

431

432 **Acknowledgments.** This research was supported by the Office of Science (BER), US  
433 Department of Energy. Todd Lane is supported by an Australian Research Council Future  
434 Fellowship (FT0990892). We would like to thank the three anonymous reviewers for their  
435 thoughtful comments and suggestions which helped to improve the manuscript greatly.

436

## References

- 437 Beres, J. H., M. J. Alexander, and J. Holton, Effects of tropospheric wind shear on the  
438 spectrum of convectively generated gravity waves, *J. Atmos. Sci.*, *59*, 1805–1824, 2002.
- 439 Berry, G. J., M. J. Reeder, and C. Jakob, Coherent synoptic disturbances in the Australian  
440 monsoon, *25*, 8409–8421, 2012.
- 441 Bretherton, C. S., Group velocity and the linear response of stratified fluids to internal  
442 heat or mass sources, *J. Atmos. Sci.*, *45*, 81–93, 1988.
- 443 Chun, H.-Y., and J.-J. Baik, Momentum flux by thermally induced internal gravity waves  
444 and its approximation for large-scale models, *J. Atmos. Sci.*, *55*, 3299–3310, 1998.

- 445 Dhaka, S. K., M. K. Yamamoto, Y. Shibagaki, H. Hashiguchi, M. Yamamoto,  
446 and S. Fukao, Convection-induced gravity waves observed by the equatorial at-  
447 mosphere radar (0.2°S, 100.32°E) in Indonesia, *Geophys. Res. Lett.*, *32*, L14,820,  
448 doi:10.1029/2005GL022,907.2, 2005.
- 449 Gardener, C. S., and N. F. Gardener, Measurement distortion in aircraft, space shuttle,  
450 and balloon observations of atmospheric density and temperature perturbation spectra,  
451 *J. Geophys. Res.*, *98*, 1023–1033, 1993.
- 452 Geller, M. A., and J. Gong, Gravity wave kinetic, potential, and vertical fluctuation  
453 energies as indicators of different frequency gravity waves, *J. Geophys. Res.*, *115*,  
454 D11,111,doi:10.1029/2009JD012,266, 2010.
- 455 Gong, J., and M. Geller, Vertical fluctuation energy in United States high vertical res-  
456 olution radiosonde data as an indicator of convective gravity, *J. Geophys. Res.*, *115*,  
457 D11,110,doi:10.1029/2009JD012,265, 2010.
- 458 Hecht, J., et al., Imaging of atmospheric gravity waves in the stratosphere and upper  
459 mesosphere using satellite and ground-based observations over Australia during the  
460 TWPICE campaign, *J. Geophys. Res.*, *114*, D18,123,doi:10.1029/2008JD011,259, 2009.
- 461 Inoue, T., A cloud type classification with NOAA 7 Split-window measurements, *J. Geo-*  
462 *phys. Res.*, *92*, 3991–4000, 1987.
- 463 Kaur, M., et al., Characteristics of Tropospheric Gravity Waves using the Equatorial At-  
464 mosphere Radar at Koto Tabang (0.20S, 100.32E), Indonesia during CPEA -2 campaign,  
465 *Atmos. Res.*, *109-110*, 84–94, 2012.
- 466 Keenan, T., K. Glasson, T. Cummings, J. Keeler, and J. Lutz, The BMRC/NCAR C-band  
467 polarimetric (C-pol) radar system, *J. Atmos. Ocean Technol.*, *15*, 871–886, 1998.

- 468 Ki, M.-O., and H.-Y. Chun, Inertia gravity waves associated with deep convection observed  
 469 during the summers of 2005 and 2007 in Korea, *J. Geophys. Res.*, *116*, D16,122, 2011.
- 470 Lane, T. P., M. J. Reeder, and T. L. Clark, Numerical modeling of gravity waves genera-  
 471 tion by deep tropical convection, *J. Atmos. Sci.*, *58*, 1249–1274, 2001.
- 472 Lane, T. P., M. J. Reeder, and F. M. Guest, Convectively generated gravity waves ob-  
 473 served from radiosonde data taken during MCTEX, *Quart. J. Roy. Meteorol. Soc.*, *129*,  
 474 D11,111, doi:10.1029/2009JD012,266, 2003.
- 475 Marks, C. J., and S. D. Eckermann, A three-dimensional nonhydro-dynamic ray-tracing  
 476 model for gravity waves: formulation and preliminary results for the middle atmosphere,  
 477 *J. Atmos. Sci.*, *52*, 1959–1984, 1995.
- 478 Nappo, C. J., *An Introduction to Atmospheric Gravity Waves*, 276 pp. pp., Academic  
 479 Press, 2002.
- 480 Reeder, M. J., N. Adams, and T. P. Lane, Radiosonde observations of partially trapped  
 481 lee waves over Tasmania, Australia, *J. Geophys. Res.*, *104*, 719–728, 1999.
- 482 Salby, M., and R. Garcia, Transient response to localized episodic heating in the tropics.  
 483 Part I: Excitation and short-time near-field behavior, *J. Atmos. Sci.*, *44*, 458–498, 1987.
- 484 Sentman, D. D., et al., Simultaneous observations of mesospheric gravity waves and sprites  
 485 generated by a midwestern thunderstorm, *J. Atmos. Sol. Terr. Phys.*, *65*, 537–550, 2003.
- 486 Steiner, M., M. J. Smith, and R. Uijlenjoet, A microphysical interpretation of radar  
 487 reflectivity-rain rate relationships, *J. Atmos. Sci.*, *61*, 1114–1131, 2004.
- 488 Uma, K. N., K. K. Kumar, and T. N. Rao, Vhf radar observed charac-  
 489 teristics of convectively generated gravity waves during wet and dry spells  
 490 of indian summer monsoon, *J. Atmos. Sol. Terr. Phys.*, *73*, 815–824, doi:

491 <http://dx.doi.org/10.1016/j.jastp.2011.01.024>, 2011.

492 Vallgren, A., Statistical characteristics of convective storms in Darwin, northern Australia,

493 Master's thesis, Lulea University of Technology, Sweden, 2006.

494 Wapler, K., and T. P. Lane, A case of offshore convective initiation by interacting land

495 breezes near Darwin, Australia, *Meteorol. Atmos. Phys.*, *115*, 123–137, 2012.

496 Xie, S., T. Hume, C. Jakob, S. A. Klein, R. B. McCoy, and M. Zhang, Observed large-

497 scale structures and diabatic heating and drying profiles during TWP-ICE, *J. Climate*,

498 *23*, 57–79, doi: 10.1175/2009JCLI3071.1, 2010.

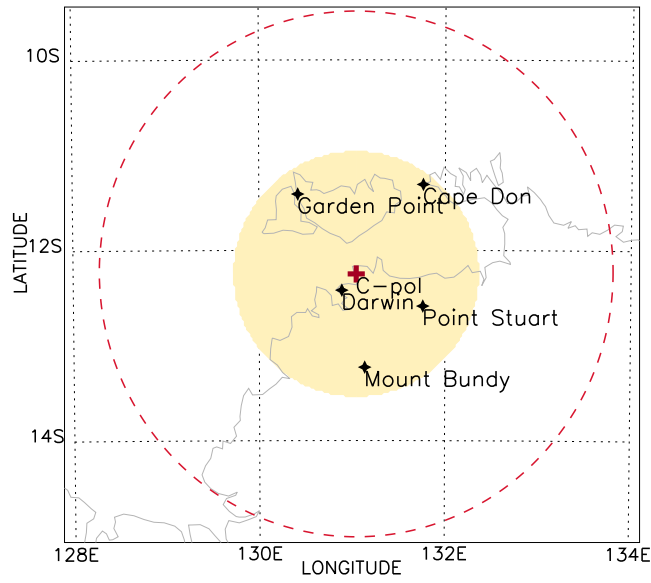


**Figure 1.** Observation sites during TWPICE. The shaded region centred at the cross sign marks the area covered by the C-pol radar data. The dashed circle shows the 300 km radius from the radar centre.

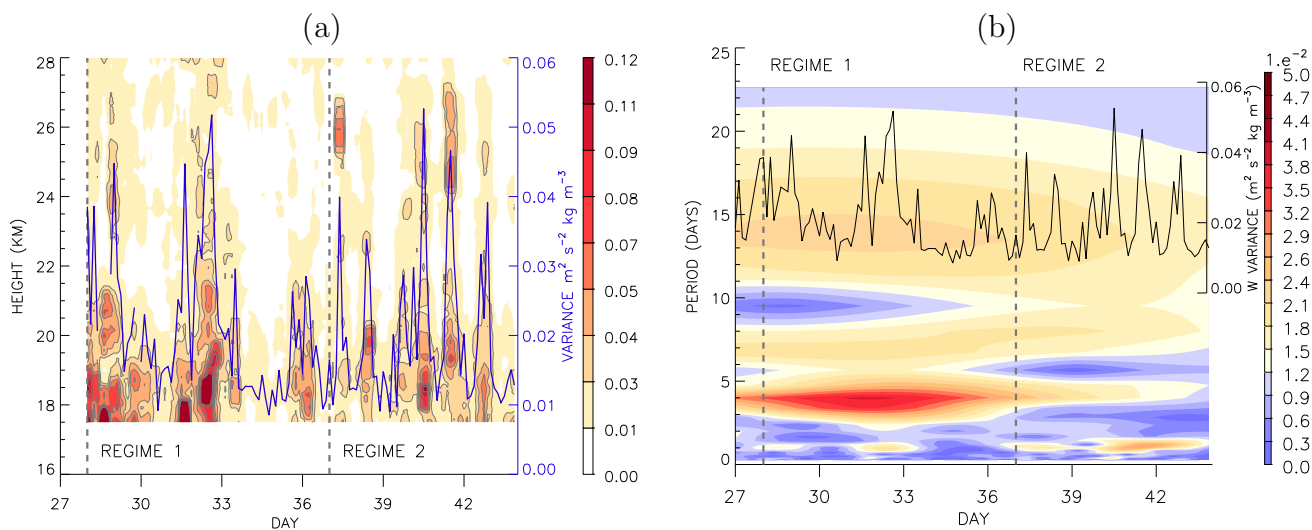


**Figure 2.** Evolution of high-frequency wave activity in the stratosphere. a) Time-height plot of  $\rho w'^2$  (shaded) and b) wavelet (Morlet) transform (shaded) of the mean wave activity  $\overline{\rho w'^2}$  (lines in both panels) in the stratosphere (17.5-28 km).

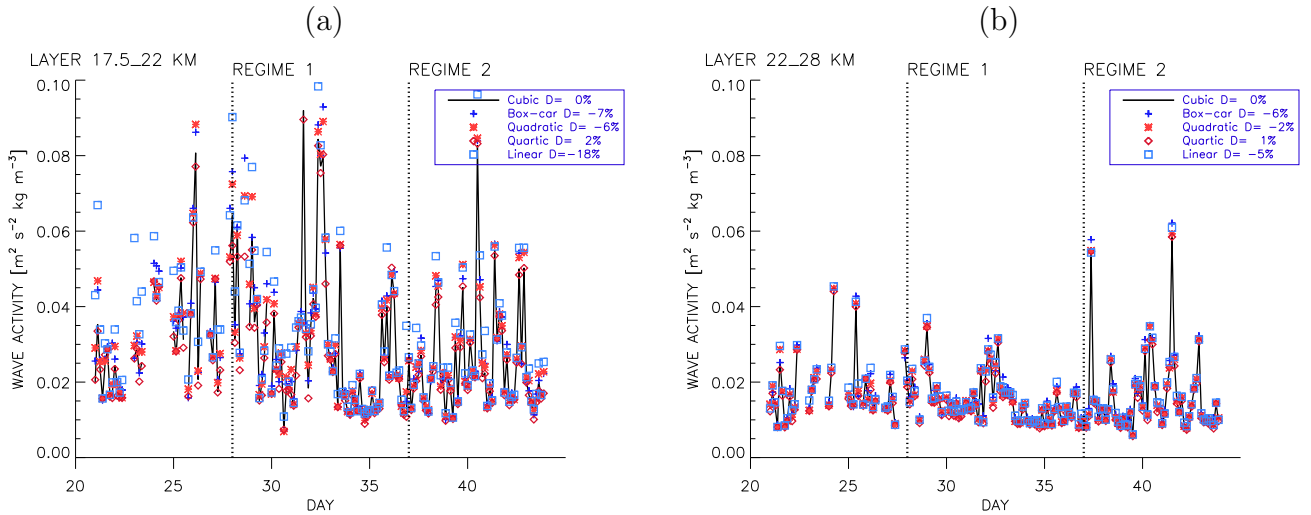


**Figure 3.** Variation of high-frequency wave activity in the stratosphere averaged for a) the 17.5-22 km layer, b) the 22-28 km layer. Perturbations of vertical velocity are calculated by removing fitted polynomials of first order (blue squares), second order (red asteriks), third order (solid line) and fourth order (red diamonds). Plus signs show the wave activity calculated by applying a 5-km box-car smoothing after a fitted cubic polynomial was removed from the vertical profiles of the balloon’s ascent rates.  $D = \langle (\rho w_{cubic}^{\prime 2} - \rho w_i^{\prime 2}) / \rho w_{cubic}^{\prime 2} \rangle$ , where  $i$  denotes the calculations with different base polynomials,  $\langle \rangle$  is the time average.

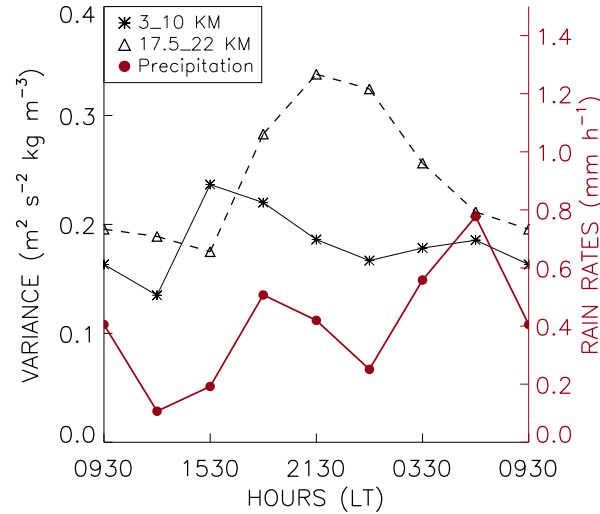


**Figure 4.** Diurnal variation of  $\overline{\rho w'^2}$  during Regime 2 in the lower stratosphere 17.5-22 km (dashed line with triangles), troposphere 3-10 km (solid line with stars), and of the area-averaged rain rates (red solid lines with circles).  $\overline{\rho w'^2}$  in the stratosphere is multiplied by 10 for clarity.

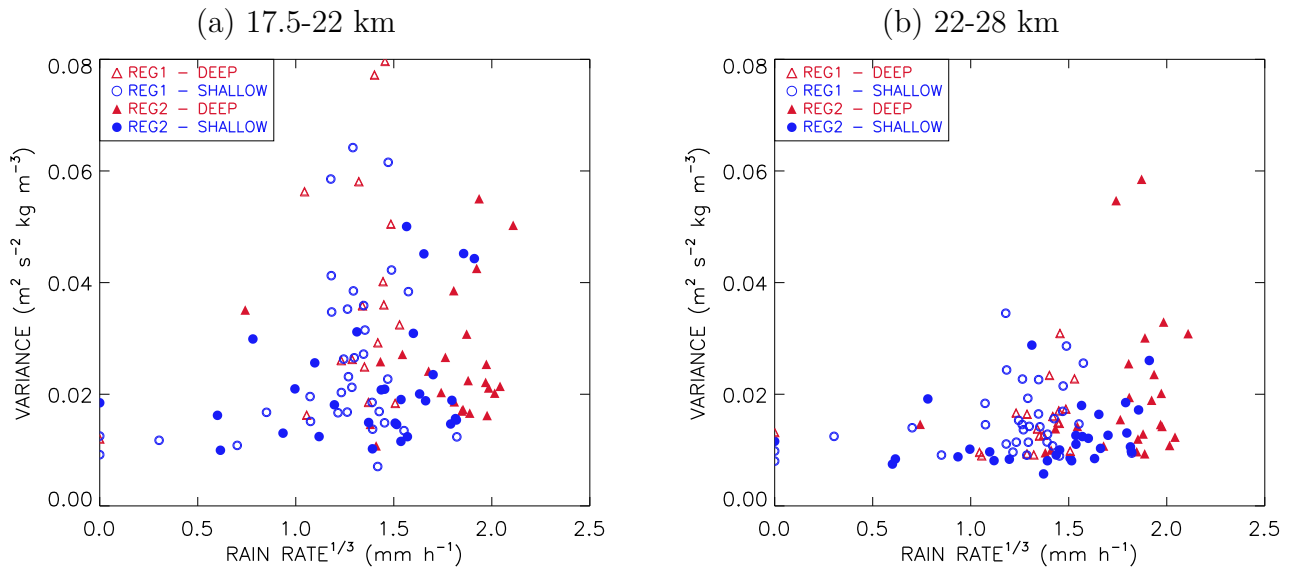


**Figure 5.** Scatter plot of  $\overline{\rho w'^2}$  during Regimes 1 and 2 in the layer (a) 17.5-22 km and (b) 22-28 km as a function of the cube root of the convective rainfall intensity. The open symbols are used for Regime 1 and the closed symbols used for Regime 2.

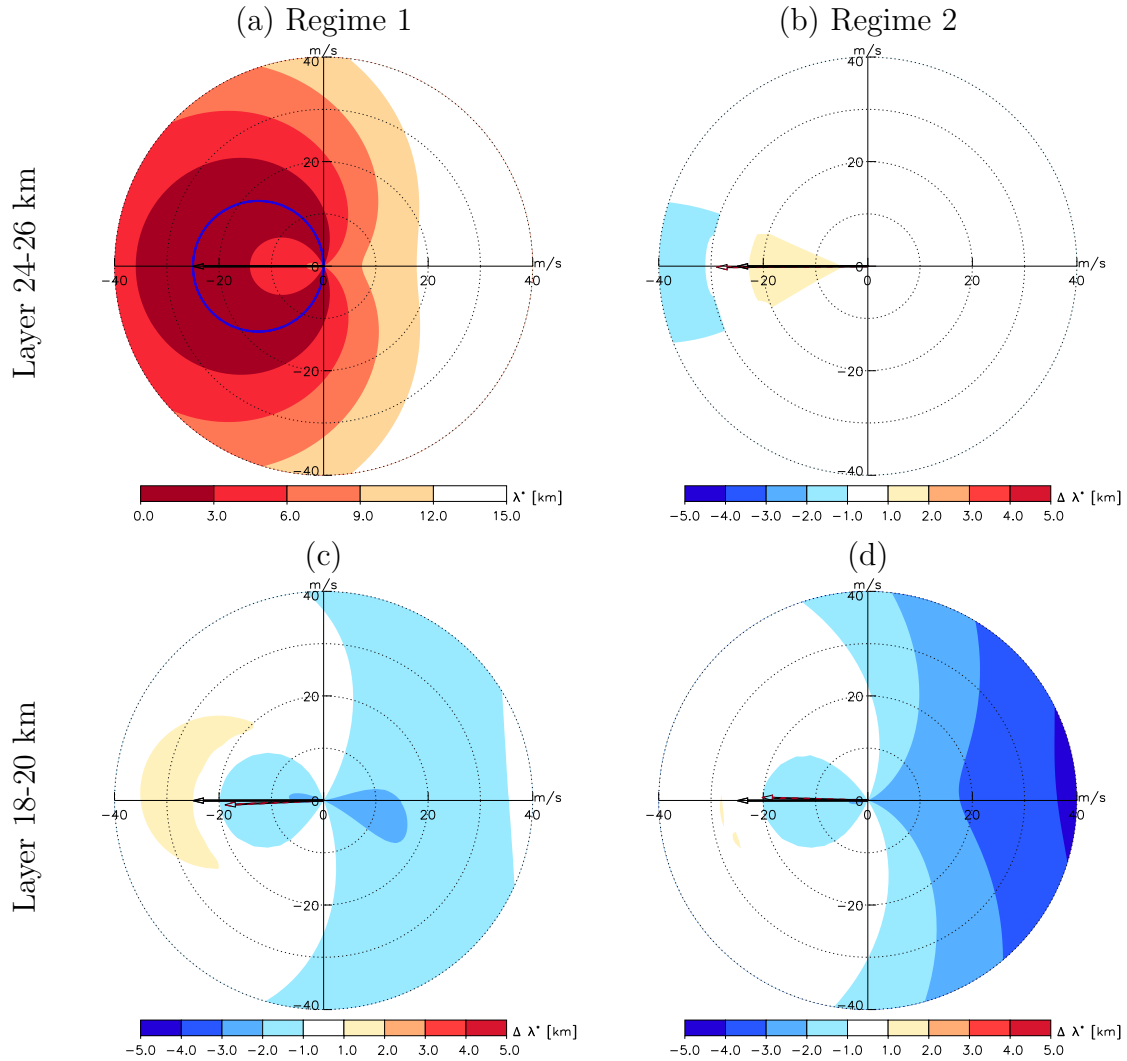


**Figure 6.** a) Critical horizontal wavelengths (shaded) for the 24-26 km layer during days 31-33 in Regime 1  $\lambda^*_{R1U}$ . The blue circle marks the critical level where  $c = U$ . The black arrow indicates the mean environmental wind. b) Difference in  $\lambda^*_{R1U}$  and  $\lambda^*$  for layer 24-26 km during days 38-40 in Regime 2  $\lambda^*_{R2U} - \lambda^*_{R1U}$ . c) and d): Similar to b) but for layer 18-20 km during days 31-33 in Regime 1  $\lambda^*_{R1L} - \lambda^*_{R1U}$  and days 38-40 in Regime 2  $\lambda^*_{R2L} - \lambda^*_{R1U}$ , respectively.

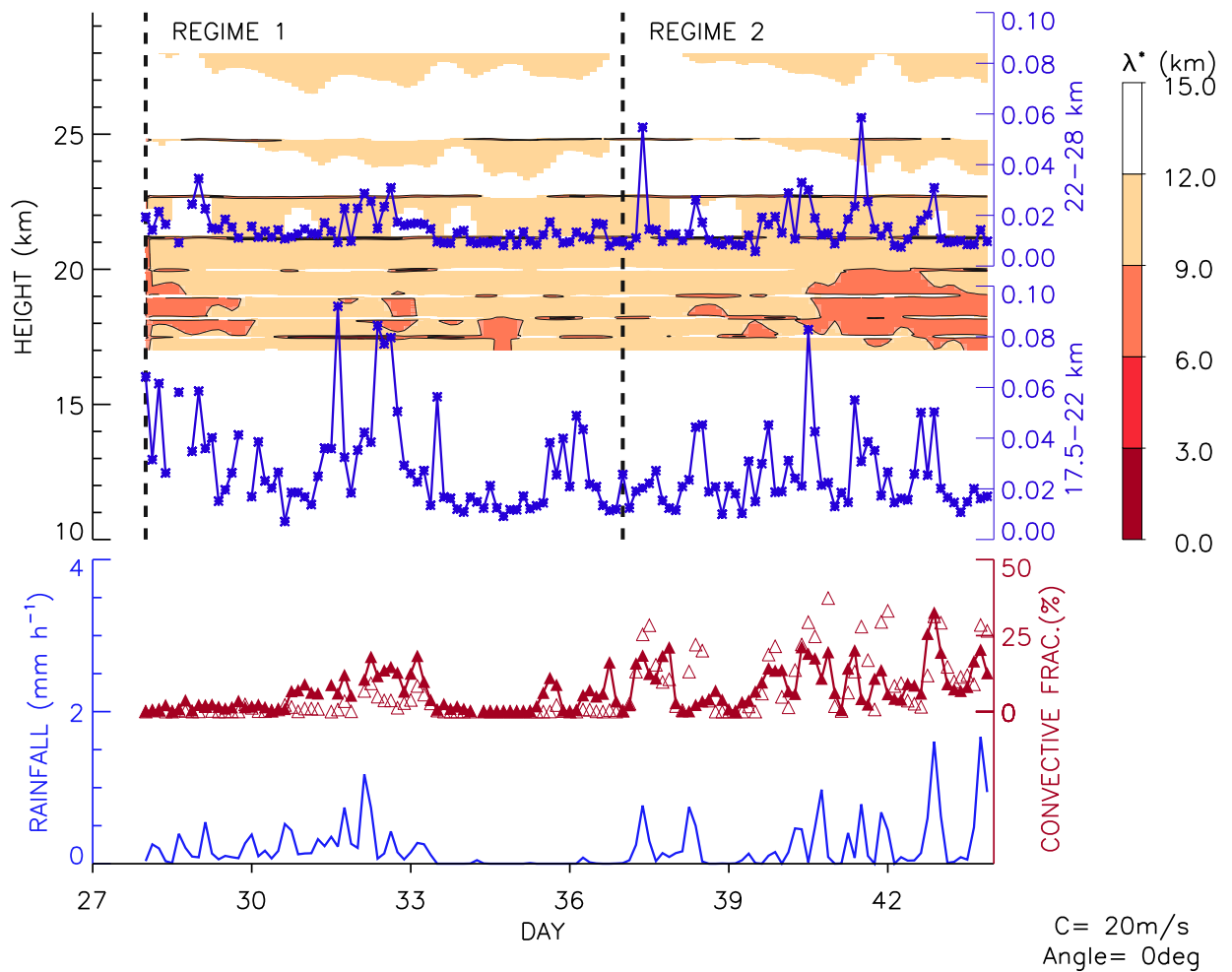


**Figure 7.** Upper panel: Evolution of the critical wavelength  $\lambda^*$  (shaded) and the wave activity  $\overline{\rho w'^2}$  in the 22-28 km layer (top line with asterisks) and the 17.5-22 km (second line from top with asterisks). Lower panel: Time series of convection coverage within 150 km radius (red open triangles) and between 150 and 300 km radii (red filled triangles) from Darwin, and the area-averaged convective rain rates (solid blue line) estimated by C-pol radar centred at Darwin.

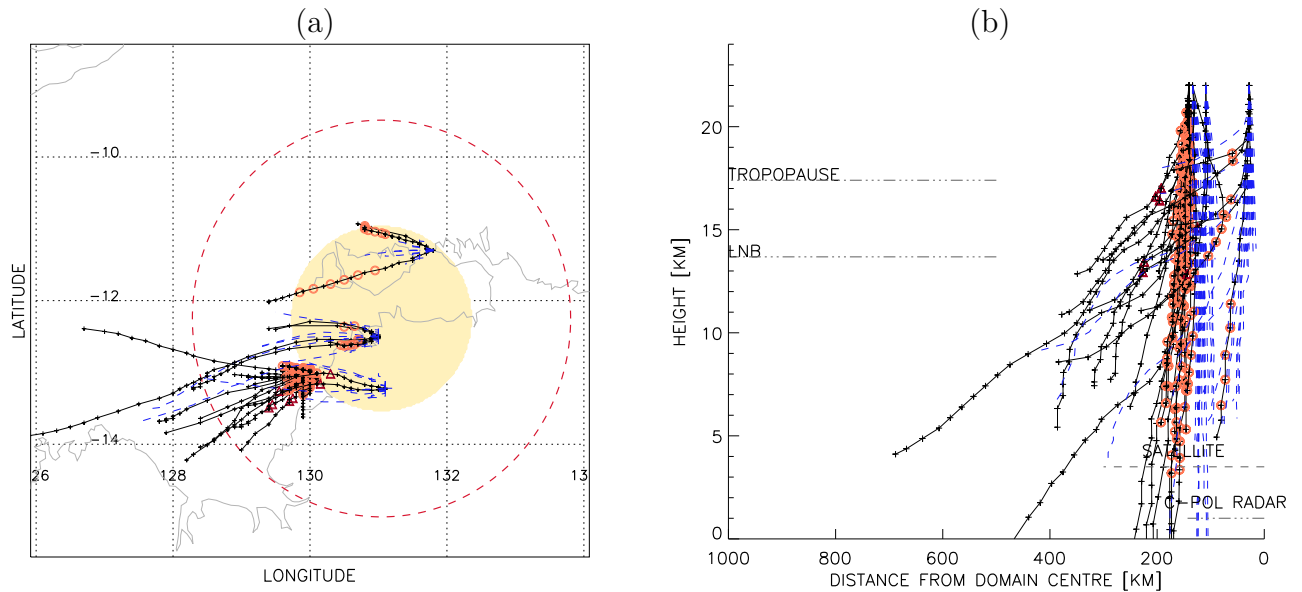


**Figure 8.** Backward ray-tracing results for 00Z day 36. Black solid (dashed blue) lines show rays that do (do not) pass over convective regions. Red triangles (brown circles) mark deep (shallow) convection. Convection is identified along a section between two consecutive points of ray paths if convection coverage is at least 10% in the  $1^\circ \times 1^\circ$  box centered in the middle of the section. Radar coverage area is shaded. Dashed red circle shows the 300-km radius, within which satellite data were used for estimating convective activity in Figure 7. (a) Horizontal plane view, (b) Distance-Height view. Distance is calculated from the location of C-Pol radar at (131.044 E, 12.249 S).

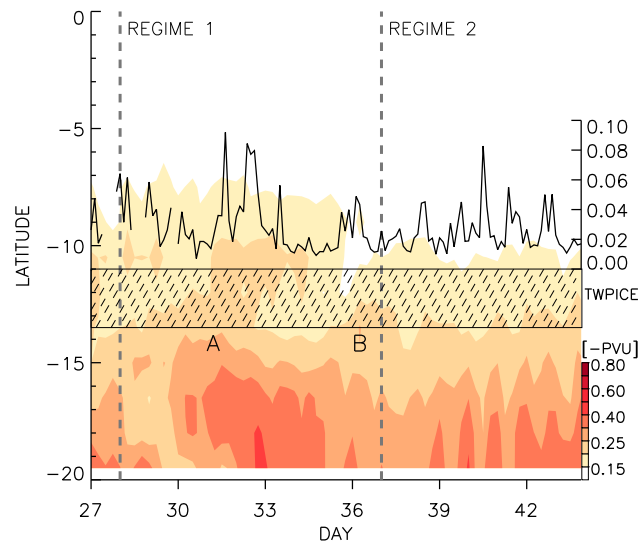


**Figure 9.** Time-latitude Hovmöller diagram (shaded) of the low-level tropospheric potential vorticity at 130°E longitude and in the layer between the 310 *K* and 320 *K* isentropic surfaces. The solid line shows the wave activity in the stratosphere (17.5–28 km) averaged over stations. Potential vorticity is calculated from the ERAI dataset with 1.5×1.5-degree horizontal resolution. Latitudes of the TWP-ICE domain are marked with the dashed box.